THE JOURNAL OF
PHYSICAL CHEMISTRY C

Article

pubs.acs.org/JPCC

Substituent Effects and Molecular Descriptors of Reactivity in Condensation and Esterification Reactions of Oxygenates on Acid–Base Pairs at TiO_2 and ZrO_2 Surfaces

Shuai Wang and Enrique Iglesia*

Department of Chemical and Biomolecular Engineering, University of California at Berkeley, Berkeley, California 94720, United States

Supporting Information

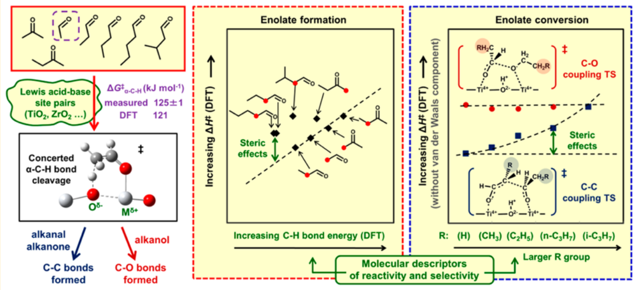

ABSTRACT: This study reports evidence for the identity and kinetic relevance of the elementary steps that mediate condensation and esterification reactions of C_2–C_5 alkanals and alkanones and for the number, role, and acid–base properties of active Ti–O and Zr–O site pairs on catalytic surfaces. Kinetic, isotopic, and theoretical methods show that all reactants convert on TiO_2 and ZrO_2 surfaces via similar routes, which involve (i) kinetically relevant α-C–H cleavage in alkanals (alkanones) to enolates on sparsely covered M–O pairs, (ii) selectivity-relevant subsequent enolate reactions with coadsorbed alkanals/alkanones or 1-alkanols to form condensation or esterification precursors, mediated by C–C coupling steps with carbonyl reactants and C–O coupling steps with alkanal–alkoxide pairs formed via H transfer in enolate–1-alkanol pairs, (iii) hydrogenation of C–C coupling products to carbonyl compounds and dehydrogenation of hemiacetals formed via C–O coupling to esters on an interspersed Cu function present as a physical mixture. For mixtures of oxygenate reactants, enolate formation rates from each reactant are unaffected by the other reactants, while C–C and C–O coupling product ratios allow measurements of the relative reactivity of each enolate with different carbonyls or alkanols; these reactivities are unavailable from carbonyl–alkanol mixtures derived from a single reactant but are essential to benchmark theory and experiment. Density functional theory (DFT) treatments on model $Ti_5O_{19}H_{18}$ clusters give free energy barriers for enolate formation ($\Delta G^{\ddagger}$) and $\Delta G^{\ddagger}$ differences for the coupling of each enolate with different alkanals, alkanones, or 1-alkanols in excellent agreement with measured values. Enthalpy and entropy components of DFT-derived activation free energy barriers show that alkyl substituents influence enolate reactivity through their effects on α-C–H bond energies and on steric hindrance at transition states (TS). Substituents influence enolate C–C coupling more strongly than C–O coupling because steric effects predominate at the tighter TS structures that mediate condensation events. Enolate formation turnover rates, based on the number of active M–O pairs measured by titration with propanoic acid during catalysis, are higher on ZrO_2 than TiO_2. Titrations during catalysis showed that the higher intrinsic reactivity of ZrO_2 reflects its weaker Lewis acid centers and more strongly basic O atoms than on TiO_2, which lead, in turn, to more stable enolate formation transition states. The different properties of the two Zr centers in Zr–O–Zr structures lead to relative C–C and C–O coupling rates that depend on the Zr center that stabilizes the O atom in enolates. This asymmetry contrasts the single-site character of Ti–O–Ti structures and leads to marked differences in the effects of alkanal/alkanol reactant ratios on condensation and esterification selectivities.

1. INTRODUCTION

Aldol condensations of carbonyl compounds form new C–C bonds and remove O atoms via steps that involve the cleavage of α-C–H bonds, nucleophilic attack of carbonyls by enolates or enols, and dehydration of the aldols formed to α,β-unsaturated carbonyl compounds.[1,2] In doing so, condensation and the mechanistically related esterification reactions form larger alkanals, alkanones, and esters from alkanol–alkanal mixtures; these products contain longer chains with fewer O atoms than reactants, making such reactions ubiquitous in the upgrading of biomass-derived oxygenates to molecules of greater value and energy density.[3−8] For instance, acetone–butanol–ethanol mixtures (ABE)[8,9] and ethanol[3] can be used as convenient renewable precursors to petrochemicals and transportation fuels.

Aldol condensations can be catalyzed by monofunctional acids and bases, resulting in enols and enolates as the respective intermediates.[10] The concerted effects of separate acid and base sites effectively stabilize the transition states that mediate the elementary steps involved in aldol condensation (α-C–H cleavage and C–C coupling steps) on biological catalysts[11] and functionalized porous silicas.[12,13] Such synergies also appear to

Received: July 20, 2016
Revised: August 26, 2016
Published: August 26, 2016

DOI: 10.1021/acs.jpcc.6b07304
J. Phys. Chem. C 2016, 120, 21589−21616

prevail on oxides (e.g., MgO,[14−16] Mg_xAlO_y,[17−20] Ce_xZrO_y,[21,22] Zn_xZrO_y,[23] and TiO_2[24−26]), which exhibit surfaces with acid−base site pairs consisting of M−O moieties (M, metal center; O, lattice oxygen atom).[27−31] Coordinative unsaturation is required at metal centers for interactions with the carbonyl group, with vicinal O atoms acting as the H abstractor, as shown by infrared evidence,[28,29] by the effects of titrants differing in acidic or basic properties,[15,30] and by theoretical treatments.[30,31] Thermodynamic hurdles, side reactions, and fast deactivation[18,25,26] have led to imprecise assessments of reactivity and of the number of active sites; these phenomena have led, in turn, to equivocal and contradictory proposals for the elementary steps and their kinetic relevance in condensation catalytic cycles.

H_2 and a Cu function, present as a mixed cocatalyst with oxides (e.g., anatase TiO_2 ($TiO_2(a)$))[30] and monoclinic ZrO_2 ($ZrO_2(m)$) shown here), circumvent the thermodynamic bottlenecks and fast deactivation ubiquitous in these reactions via hydrogenation of unsaturated products and dehydrogenation of hemiacetals to complete catalytic turnovers that form stable products; these bifunctional strategies also allow the interchangeable use of alkanals/alkanones and their respective alkanols as reactants via their fast equilibration. Our previous study[30] demonstrated the role of Ti−O Lewis acid−base site pairs on $TiO_2(a)$ in stabilizing enolate formation transition states (TS) in the conversion of C_3 oxygenates. These enolates then react with carbonyl molecules to form C−C bonds and with 1-alkanols to form alkanal−alkoxide pairs that form C−O bonds, thus completing condensation and esterification turnovers. The number of active acid−base site pairs, measured by titration with propanoic acid during catalysis, allowed measurements of intrinsic site reactivities and the benchmarking of activation free energies and mechanistic conclusions against density functional theory (DFT) estimates.[30]

The kinetic, isotopic, and theoretical assessments shown here demonstrate the general nature of these mechanistic conclusions for diverse C_2−C_5 oxygenates on $TiO_2(a)$ and also on $ZrO_2(m)$. Site titrations with CO_2, pyridine, and propanoic acid during catalysis confirm that Ti−O and Zr−O acid−base site pairs of moderate acid−base strength preferentially stabilize enolate transition states that involve concerted interactions with O and Ti or Zr centers. Esterification/condensation rate ratios on $ZrO_2(m)$ depend weakly on alkanol/alkanal ratios, in contrast to the linear relations observed on $TiO_2(a)$ surfaces with uniform Ti centers.[30] Such differences reflect distinct Zr sites on Zr−O−Zr structures, which predominantly lead to the formation of C−C or C−O bonds, depending on the specific Zr center used to stabilize the enolate at the bimolecular transition states that mediate these reactions.

Detailed studies of the formation rates of various products from mixtures of different alkanals/alkanones led to rigorous assessments of the relative reactivity of different carbonyl compounds and 1-alkanols with enolates, which cannot be extracted from carbonyl−alkanol mixtures derived from a single reactant. C−C bond formation rates of alkanals with a given enolate depend weakly on alkanal size or substitution but are significantly higher than for alkanone reactions with the same enolate, as a result of steric effects brought forth by the alkyl substituents at carbonyl C atoms in nucleophilic attack reactions by enolates. H_2O does not inhibit enolate formation rates but acts as an esterification cocatalyst via its reaction with enolates to form 1,1-diols, which undergo rapid etherification with alkanols to form hemiacetals and H_2O.

Theoretical treatments on model anatase clusters accurately describe the effects of molecular identity on enolate formation rates and on the selectivity for C−C and C−O formation steps of enolates for C_2−C_5 oxygenates. These treatments and data are useful in constructing kinetic models to describe rates and selectivities in complex mixtures of alkanols and carbonyl compounds. DFT-derived enthalpy and entropy components of activation free energy barriers confirmed that enolate formation rates depend on α-C−H bond energies and on repulsive interactions that inhibit reactivity when alkyl substituents are present at the α-C atom. Steric effects of alkyl substituents at the carbonyl C atom of alkanal/alkanone reactants are the sole descriptor of the relative rates of esterification and condensation for each enolate and reflect transition states that are much tighter for C−C coupling than for C−O coupling.

2. METHODS

2.1. Catalyst Synthesis and Characterization. TiO_2 Degussa P25 (99.8%, 50 m^2 g^{-1}, anatase/rutile = 3/1 mass) was used as a catalyst; its condensation and esterification reactivity arises exclusively from anatase surfaces[30] and is hereinafter denoted as $TiO_2(a)$. It was treated at 673 K (0.167 K s^{-1}) for 3 h in flowing dry air (1.67 cm^3 g^{-1} s^{-1}, 99.999%, Praxair) and then physically mixed with Cu/SiO_2 (ca. 20% wt Cu) catalysts[30] using a mortar and pestle. The mixtures ($TiO_2(a)$ + Cu/SiO_2, 0−4 (Cu/SiO_2)/TiO_2 mass ratio) were pressed into pellets, crushed, and sieved to prepare 180−250 μm aggregates. These mixtures are used to circumvent the thermodynamic, selectivity, and stability hurdles ubiquitous in condensation and esterification reactions.[30]

Monoclinic ZrO_2 ($ZrO_2(m)$, 131 m^2 g^{-1}) was also used as a catalyst; it was prepared using hydrothermal methods.[32] $ZrO(NO_3)_2 \cdot xH_2O$ (99.99%, Sigma-Aldrich) and urea ($CO(NH_2)_2$, 99%, Aldrich) were dissolved in 60 cm^3 of deionized water (0.40 mmol cm^{-3} Zr^{4+}, urea/Zr^{4+} = 10 mol). The solution was placed in a Teflon-lined stainless-steel autoclave (100 cm^3) and held stagnant at 433 K for 20 h under its autogenous pressure. The solids formed were washed with deionized water until the filtrate reached a neutral pH and then treated in ambient air at 383 K (0.167 K s^{-1}) overnight and in flowing dry air (1.67 cm^3 g^{-1} s^{-1}, 99.999%, Praxair) at 673 K (0.167 K s^{-1}) for 4 h. This catalyst was physically mixed with the Cu/SiO_2 catalysts, as described above ($ZrO_2(m)$ + Cu/SiO_2, 1:1 mass, 180−250 μm).

The Cu/SiO_2 synthesis protocols were described elsewhere.[30] They involved treating an aqueous suspension of colloidal silica (30% wt LUDOX SM-30), $Cu(NO_3)_2 \cdot 2.5H_2O$ (99.99%, Sigma-Aldrich), and urea (99%, Aldrich) (Cu/urea = 1/3 mol) at 363 K for 20 h while stirring. The powders were rinsed with deionized water to a neutral filtrate pH and treated in ambient stagnant air at 383 K for 20 h, then in flowing dry air (1.67 cm^3 g^{-1} s^{-1}, 99.999%, Praxair) at 723 K for 5 h, and finally in flowing 10% H_2/He (5.56 cm^3 g^{-1} s^{-1}, 99.999%, Praxair) at 573 K for 2 h. A treatment in flowing 1% O_2/He (0.83 cm^3 g^{-1} s^{-1}, 99.999%, Praxair) at ambient temperature for 1 h was used to passivate the samples before exposure to ambient air. The line breadth in X-ray diffractograms gave a mean Cu diameter of 7.9 nm.[30]

2.2. Catalytic Rate Measurements. C_2−C_5 oxygenates and their mixtures were used as reactants; these oxygenates included ethanol (>99.9%, Fisher), ethanol-d_6 (>99.96%, Sigma-Aldrich), 1-propanol (>99.9%, Sigma-Aldrich), 2-propanol (>99.5%, Sigma-Aldrich), acetone (>99.9%, Fisher), acetone-d_6 (>99.9%, Aldrich), 1-butanol (>99.8%, Sigma-Aldrich), 2-butanol (>99.5%, Sigma-Aldrich), 1-pentanol (>99.0%, Sigma-Aldrich), and 3-methyl-1-butanol (>99.0%, Sigma-Aldrich). Their conversion rates and selectivities were measured on $TiO_2(a)$ + Cu/SiO_2 and $ZrO_2(m)$ + Cu/SiO_2 mixtures (10−500 mg) using a quartz tubular flow reactor (1.0 cm i.d.). The catalyst mixtures were treated in flowing 10% H_2/He (5.56 $cm^3\ g^{-1}\ s^{-1}$, 99.999%, Praxair) at 543 K (0.0833 K s^{-1}) for 2 h before contact with reactants. The liquid reactants were vaporized by introducing them into a stream of He (99.999%, Praxair) and H_2 (99.999%, Praxair) mixtures with all transfer lines after the point of introduction held at 433 K. H_2 was replaced by D_2 (99.8%, Praxair) when deuterated oxygenates were used as reactants. Reactant pressures and space velocities were varied by controlling the liquid and gas flow rates using syringe pumps (Cole Parmer, 74900 series) and electronic mass flow controllers (Porter, model 201), respectively.

The speciation of reaction products was carried out using known standards and mass spectrometry (HP 5972) after chromatographic separation (HP 5890 GC) with a methyl silicone capillary column (Agilent, HP-1, 50 m, 0.32 mm i.d. × 1.05 μm). The concentrations of reactants and products in the effluent stream were measured by online gas chromatography (Agilent 6890) using the same capillary column but with a flame ionization detector calibrated using response factors determined from known standard compounds. Equilibrated mixtures of alkanol−alkanal/alkanone reactants formed on $TiO_2(a)$ + Cu/SiO_2 or $ZrO_2(m)$ + Cu/SiO_2 at all H_2 pressures were treated as lumped reactants that are hereinafter denoted as the reactant pool; pool conversions and product selectivities are based on the molecules that leave this pool (on a carbon basis). Reaction rates are normalized by the number of accessible acid−base site pairs on $TiO_2(a)$ (3.7 nm^{-2})[30] or $ZrO_2(m)$ (6.0 nm^{-2}, shown in section 3.2), determined by titration with propanoic acid during acetone condensation at 453 K (section 2.3).

2.3. Titration of Surface Sites by Probe Molecules during Catalysis.

The number and type of active sites involved in C−H bond activation steps leading to enolate intermediates on $TiO_2(a)$[30] and $ZrO_2(m)$ were determined by in situ titrations with pyridine (>99.9%, Sigma-Aldrich), propanoic acid (>99.5%, Sigma-Aldrich), and CO_2 (50% CO_2/He, 99.999%, Praxair). Acetone condensation rates were first measured here on $ZrO_2(m)$ + Cu/SiO_2 mixtures (1:1 mass) without the titrants (523 K, 4 kPa acetone, 40 kPa H_2) for 2 h. Titrants were then introduced by mixing them with acetone for liquid titrants (0.005 or 0.05 titrant/acetone molar; 20 or 200 Pa) or as a separate stream for CO_2 (4 kPa). Reactant, product, and titrant concentrations were determined by the chromatographic protocols described in section 2.2. The number of Zr−O site pairs on $ZrO_2(m)$ was determined from the propanoic acid uptakes required to suppress reactant conversion rates using a stoichiometry of one acid per two vicinal Zr−O site pairs, as required for dissociative adsorption to form carboxylates, based on theoretical[33] and infrared[34] evidence.

2.4. Density Functional theory (DFT) Methods.

A Ti_5O_{19} cluster extracted from anatase (101) surface, the most stable and prevalent exposed plane, was used to represent Ti−O site pairs; the anatase structure was set based on crystallographic data (tetragonal, $I4_1/amd$, $a = b = 0.378$ nm, $c = 0.949$ nm).[30] Two Ti_{5c} sites (coordination number (CN) 5) and one O_{3c} site (CN 3) centered in the cluster are used as the active sites (Scheme 1), as described elsewhere,[30] with the remaining O and Ti atoms providing the nonlocal coordination and electronic environment. Eighteen H atoms were bound to the edge O atoms of the cluster along the orientation of the Ti−O bonds cleaved to extract the cluster from the extended anatase structure in order to maintain the cluster charge neutral and avoid extraneous H-bonding interactions at reactant and transition states. These $Ti_5O_{19}H_{18}$ clusters provide computationally tractable model surfaces that were shown to accurately assess the kinetically relevant steps and estimate the activation free energy barriers for the formation of enolates in esterification and condensation reactions of C_3 oxygenates.[30] Similar theoretical protocols are extended here to describe the effects of molecular identity and structure on reactivity and selectivity and on the kinetic relevance of specific elementary steps for reactants consisting of a much broader range of oxygenates.

Scheme 1. $Ti_5O_{19}H_{18}$ Cluster Model for Theoretical Treatments of Aldol Condensation and Esterification Pathways

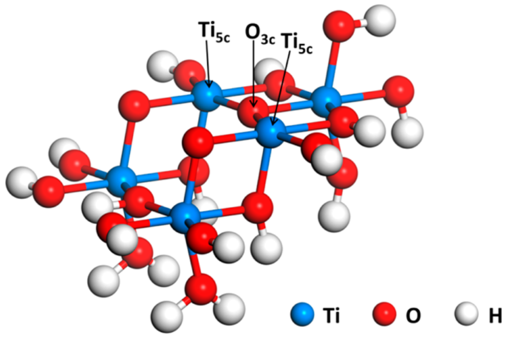

These theoretical methods used the Gaussian 09 program.[35] All five Ti atoms and the three inside O atoms in the $Ti_5O_{19}H_{18}$ cluster were relaxed, while the remaining atoms were held to preserve the structure of the extended anatase parent surface. Geometry optimization of reactants, products, and transition states (TS) used the Berny geometry algorithm[36] at the hybrid B3LYP functional level of theory[37,38] with the Gaussian-type 6-311G(d,p) basis set for the C, O, and H atoms[39,40] and the effective core potential LANL2DZ basis set for the Ti atoms.[41] An ultrafine grid (99590) was selected for numerical integration; convergence criteria were set to 1.0×10^{-8} Ha for energy and 1.5×10^{-5} Ha $Bohr^{-1}$ for the maximum residual force on each atom. The van der Waals contributions to electronic energies of optimized structures were estimated by Grimme's D3BJ dispersion correction,[42] and basis set superposition errors (BSSE) were treated using the counterpoise correction method to eliminate overestimation of binding energies as a result of basis-function overlaps for the finite basis sets used.[43,44]

Enthalpies and entropies were calculated based on the vibrational partition functions derived from the rigid rotor harmonic oscillator (RRHO) approximation[45] using DFT-determined frequencies; these frequencies were scaled by a factor of 0.9682 to compensate for anharmonicity effects absent in the theoretical treatments.[46] For low-frequency modes (<100 cm^{-1}) of weakly bound adsorbates, vibrational partition functions were calculated using a free-rotor model instead of the RRHO model to avoid significant errors caused by the latter.[47] Bonding properties of all reactants and TS structures were analyzed using the Wiberg bond-order index[48,49] (implemented in the NBO 3.0 program[50]) that calculates bond orders based on the most possible Lewis electronic structures.

The acid–base strength of exposed Zr–O site pairs on $ZrO_2(m)$ surfaces was described using the affinities of these sites for OH^- or H^+ gaseous ions using formalisms and methods described previously.[30] The OH^- affinity (E_{HA}) reflects the energy released upon binding a gaseous OH^- at a Lewis acid center (A)

$$E_{HA} = E_{AOH^-} - E_A - E_{OH^-} \tag{1}$$

The H^+ affinity (E_{PA}) reflects the energy released upon binding a gaseous H^+ at a basic site (B)

$$E_{PA} = E_{HB^+} - E_B - E_{H^+} \tag{2}$$

Here, E_i is the electronic energy of species i. These affinities for the most stable (−111) surfaces of monoclinic ZrO_2[51] were calculated using periodic slab models, because the presence of distinct Zr and O sites precludes the use of the small cluster models that were adequate to describe single-site $TiO_2(a)$ surfaces.[30]

Energy and geometry optimizations of periodic neutral ZrO_2 slabs with and without adsorbed H^+/OH^- pairs were performed using periodic plane-wave DFT methods, as implemented in the Vienna ab initio Simulation Package (VASP).[52−54] These calculations used the Perdew–Burke–Ernzerhof (PBE) exchange-correlation functional[55,56] and projector augmented-wave (PAW) pseudopotentials[57,58] for all atoms (400 eV energy cutoff). Bulk $ZrO_2(m)$ structures were optimized using a 4 × 4 × 4 k-point mesh of the first Brillouin zone generated from the Monkhorst-pack sampling method;[59] lattice parameters measured from neutron powder diffraction ($P2_1/c$, $a = 0.515$ nm, $b = 0.521$ nm, $c = 0.532$ nm)[60] were used to construct initial structures. All atoms were allowed to relax until electronic energies varied by less 1×10^{-5} eV and forces on each atom were below 0.02 eV $Å^{-1}$. DFT-optimized lattice parameters ($a = 0.522$ nm, $b = 0.528$ nm, $c = 0.539$ nm) were determined from correlations between electronic energy and volume of the bulk structures by using the Birch–Murnaghan equation of state;[61] these parameters were 1.4% larger than the starting values derived from crystallography.

These DFT-optimized structures were used to construct 2 × 2 supercells of the (−111) surfaces as slab models for the calculations of OH^- and H^+ affinities; each unit cell consisted of four Zr_4O_8 layers along the z direction and contained 64 Zr and 128 O atoms. These periodic slabs were separated by 1.5 nm vacuum layers in the z direction. The atoms in the bottom layer of these slabs were fixed at their bulk positions, while the others were allowed to relax in all energy optimizations. A 4 × 4 × 1 Monkhorst-pack sampling k-point set and the energy and force convergence criteria described above were used in all optimizations. At each optimization step, dipole and quadrupole corrections were used to account for interactions among periodic images.[62,63] The Grimme's D2 dispersion correction was used to describe dispersion forces.[64]

3. RESULTS AND DISCUSSION

3.1. Turnover Rates and Selectivities on Anatase TiO_2 Surfaces.

Ethanol reaction rates and selectivities were measured on physical mixtures of $TiO_2(a)$ and 20% wt Cu/SiO_2 catalysts (0–4 $(Cu/SiO_2)/TiO_2$ mass ratio; 523 K, 30 kPa H_2). The approach to equilibrium factor (η_{dehy}) for alkanol dehydrogenation to alkanal (alkanone) is given by

$$\text{alkanol} \overset{K_{dehy}}{\rightleftharpoons} \text{alkanal(alkanone)} + H_2 \tag{3}$$

$$\eta_{dehy} = \frac{P_{H_2} \times P_{Alkanal(Alkanone)}}{P_{Alkanol}} \times \frac{1}{K_{dehy}} \tag{4}$$

where K_{dehy} is the equilibrium constant for the dehydrogenation reaction. The η_{dehy} value for ethanol dehydrogenation, determined from available thermodynamic data,[65] increased as the $(Cu/SiO_2)/TiO_2$ mass ratio increased and reached unity for catalyst mass ratios above unity (Figure 1), indicative of full ethanol–ethanal–H_2 equilibration. Such rapid equilibration renders alkanals and alkanols equivalent as reactants; their mixtures can therefore be rigorously treated as a single reactant lump in all kinetic treatments.

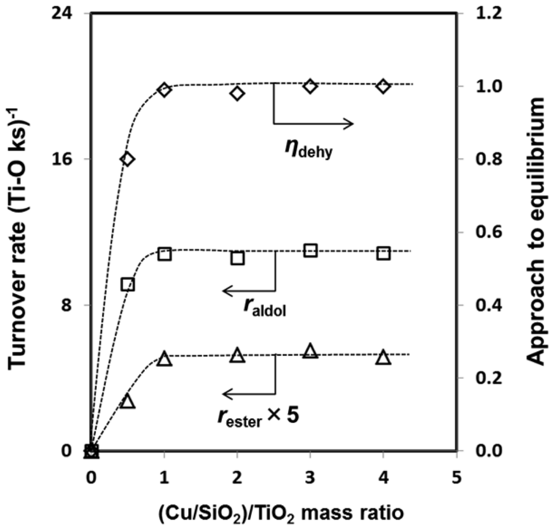

Figure 1. Effects of $(Cu/SiO_2)/TiO_2$ mass ratio on rates of aldol condensation (r_{aldol}) and esterification (r_{ester}) and the alkanol dehydrogenation approach to equilibrium factor (η_{dehy}; eq 4) for ethanol–ethanal reactants ($TiO_2(a)$ + 20% wt Cu/SiO_2, 0–4 $(Cu/SiO_2)/TiO_2$ mass ratio, 523 K, 0.8 kPa ethanol, 30 kPa H_2). Dashed lines indicate trends.

This equilibrated ethanol–ethanal reactant pool formed C_{4+} products (e.g., butanal, hexanal, and 2-ethyl-butanal) via ethanal aldol condensation and subsequent hydrogenation; it also formed ethyl acetate via dehydrogenation of hemiacetals derived from ethanol–ethanal coupling reactions (Scheme 2). Condensation and esterification turnover rates (per active Ti–O site pair) were insensitive to the amount of Cu for $((Cu/SiO_2)/TiO_2)$ mass ratios larger than unity (Figure 1). These data indicate that kinetically relevant steps occur on $TiO_2(a)$ surfaces, with the Cu function serving to equilibrate the alkanol–alkanal reactants. This Cu function also removes thermodynamic hurdles by hydrogenating unsaturated condensation products and dehydrogenating hemiacetals,[30] thus avoiding yield losses and deactivation processes mediated by subsequent reactions of the initial condensation and esterification products.

Combined aldol condensation and esterification rates of ethanol–ethanal mixtures were proportional to ethanal pressure but unaffected by ethanol pressure (Figure 2a);

Scheme 2. Reaction Network for the Conversion of Alkanols ($C_nH_{2n+1}OH$) and Its Equilibrated Carbonyl Analogs ($C_nH_{2n}O$) on Bifunctional $TiO_2(a)$ + Cu/SiO_2 Catalysts[a]

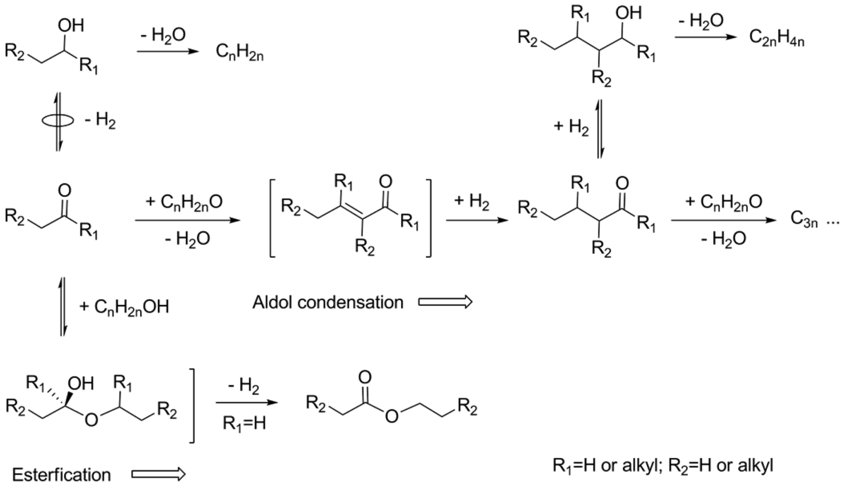

[a]The products in brackets were below the experimental detection limit (0.001 kPa).

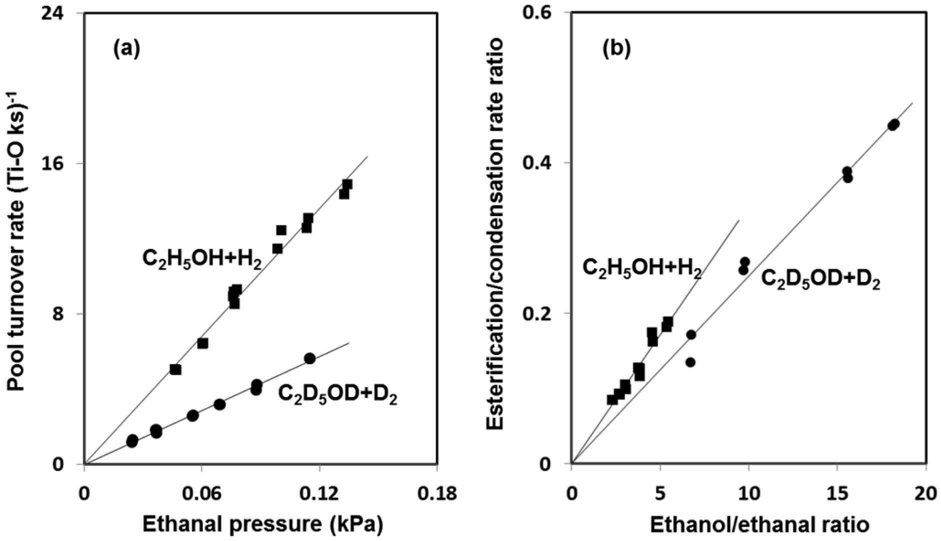

Figure 2. Effects of (a) ethanal pressure on pool turnover rates and (b) ethanol/ethanal ratio on ratios of esterification and condensation rates (523 K, $TiO_2(a)$ + 20% wt Cu/SiO_2 (1:1 mass), 0.8 kPa ethanol/ethanol-d_6, 10−60 kPa H_2/D_2). Solid lines in a and b represent the regression fits to the functional forms of eqs 5 and 6, respectively.

esterification/condensation rate ratios, in contrast, increased linearly with increasing ethanol/ethanal ratios (Figure 2b). These pressure effects on conversion rates and selectivities resemble those observed for 1-propanol−propanal reactant mixtures in a previous study,[30] suggesting that mechanistic features are similar for all these reactants, as confirmed by the evidence from experiment and theory described in the sections that follow.

A plausible sequence of elementary steps is shown in Scheme 3 for aldol condensation and esterification reactions of C_2−C_5 alkanol−alkanal reactants on M−O site pairs (e.g., M = Ti or Zr) at oxide surfaces ($TiO_2(a)$ used here as the illustrative example). These steps are consistent with all rates and selectivities measured (shown below) and with DFT-derived free energies (section 3.5) for all C_2−C_5 oxygenate reactants.

An adsorbed alkanal, present at low coverages during catalysis, undergoes α-H-abstraction by a basic lattice O atom; the incipiently formed enolate moiety at the transition state (TS) is stabilized via concerted interactions with a Lewis acid center (step 2, Scheme 3). Another alkanal, coadsorbed on a vicinal M site, is then nucleophilically attacked by the enolate species to form the new C−C bond (steps 4−6, Scheme 3); the aldol that forms dehydrates to an α,β-unsaturated carbonyl compound (step 7, Scheme 3), which is hydrogenated to the corresponding alkanones, alkanals, and alkanols on Cu sites. The enolate can also react via reversible H-abstraction with a vicinal coadsorbed alkanol to form an alkanal−alkoxide pair (step 9, Scheme 3), which forms the new C−O bond via subsequent nucleophilic attack (steps 10−12, Scheme 3); the hemiacetal formed then dehydrogenates to an ester on the Cu function (step 13, Scheme 3), thus completing an esterification turnover.

The linear rate dependence on the pressure of the carbonyl component (Figure 2a), the normal H/D isotope effects (shown below), and the DFT-derived free energies (section 3.5) require that enolate formation (step 2, Scheme 3) be the

DOI: 10.1021/acs.jpcc.6b07304
J. Phys. Chem. C 2016, 120, 21589−21616

Scheme 3. Aldol Condensation and Esterification Pathways for C_2−C_5 Alkanol−Alkanal Reactants (CH_2RCH_2OH−$CH_2RCH{=}O$, R = H or alkyl) on Bifunctional $TiO_2(a)$ + Cu/SiO_2 Mixtures[a]

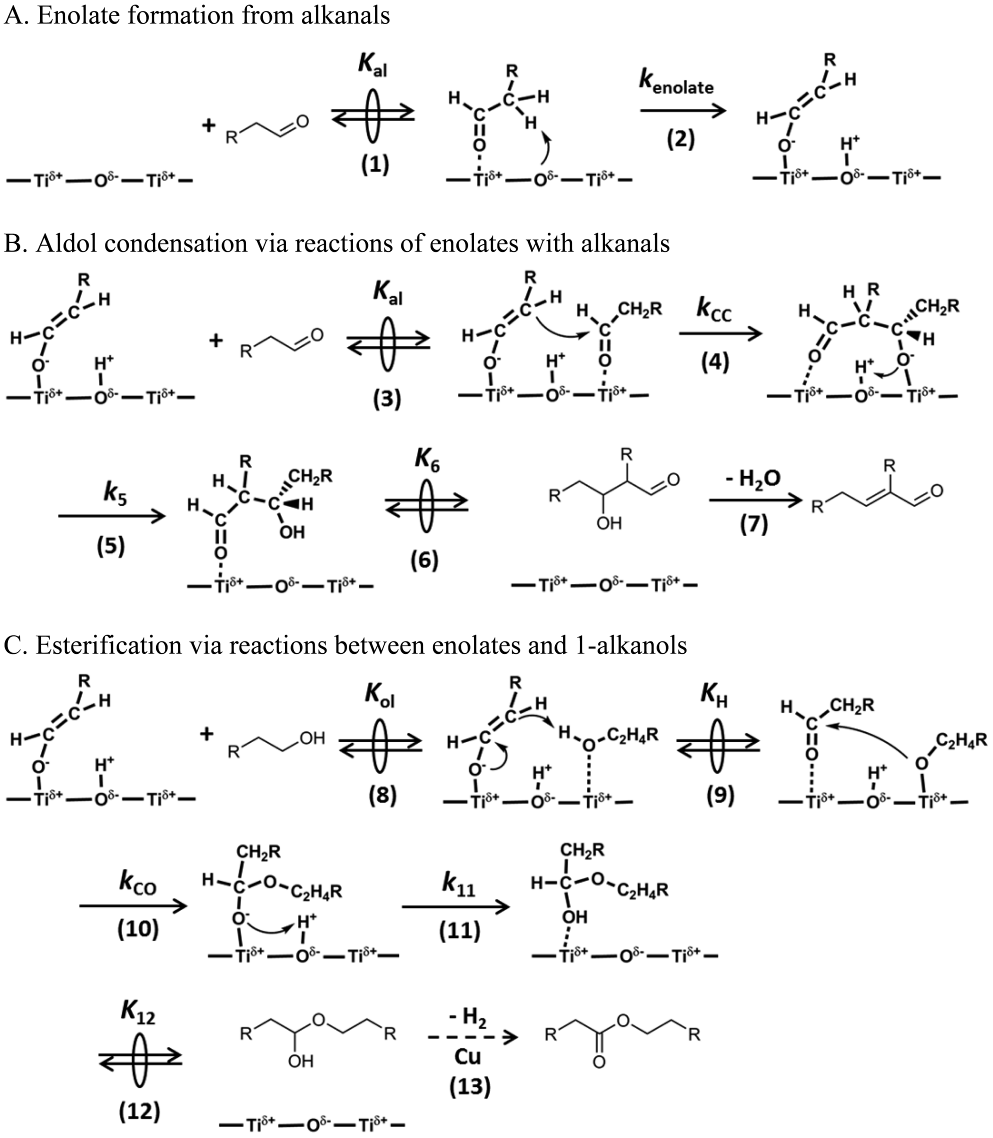
A. Enolate formation from alkanals

B. Aldol condensation via reactions of enolates with alkanals

C. Esterification via reactions between enolates and 1-alkanols

[a]Reactions on Ti−O site pairs and Cu surfaces are represented by solid and dashed arrows, respectively. Quasi-equilibrated steps are noted by a circle over double arrows. Reaction numbers used throughout the text are in parentheses (e.g., (1)); the k_j and K_j (j = 1−13) labels above each reaction arrow represent their respective kinetic constants for forward steps and equilibrium constants.

sole kinetically relevant step. The relative rates of enolate−alkanal C−C coupling (step 4, Scheme 3) and alkanal−alkoxide C−O coupling (step 10, Scheme 3) determine only the fate of the enolate species formed and thus the relative rates at which enolates ultimately appear as condensation or esterification products, consistent with the observed effects of ethanal and ethanol pressures (Figure 2b), the weak H/D isotope effects (shown below), and the DFT treatments of these enolate conversion elementary steps (section 3.5).

The sequence in Scheme 3 gives mechanism-based equations for enolate formation rates

$$\frac{r_{enolate}}{[L]} = \frac{r_{aldol} + r_{ester}}{[L]} = k_{enolate} K_{al} P_{alkanal} = k'_{enolate} P_{alkanal} \tag{5}$$

and for the ratio of esterification to condensation rates

$$\frac{r_{ester}}{r_{aldol}} = \frac{k_{CO} K_{ol} K_H P_{alkanol}}{k_{CC} K_{al} P_{alkanal}} \tag{6}$$

Here, $[L]$ is the number of active M−O site pairs on oxide surfaces, $r_{enolate}$, r_{aldol}, and r_{ester} denote the respective rates of enolate formation, aldol condensation, and esterification, the $k_{enolate}$, k_{CC}, and k_{CO} parameters represent the first-order rate constants for enolate formation (step 2), C−C coupling (step 4), and C−O coupling (step 10), $k'_{enolate}$ is the effective rate constant for enolate formation, K_{ol} and K_{al} are the adsorption constants for alkanol and alkanal reactants on metal centers, and K_H is the equilibrium constant for H transfer between alkanols and enolates (step 9, Scheme 3).

The $k'_{enolate}$ parameter in eq 5 represents the slope of the conversion rates shown in Figure 2a; it reflects the reactivity of the carbonyl molecule in the formation of enolate species (step 2, Scheme 3) via concerted α-H abstraction (by lattice O sites)

Table 1. Number of α-H Atoms ($n_{\alpha\text{-H}}$), Measured k'_{enolate}, $k_{CO}K_{ol}K_H(k_{CC}K_{al})^{-1}$, and ΔG Values for Enolate Formation, Esterification, and Condensation Reactions of C_2–C_5 Alkanal and Alkanone Reactants on $TiO_2(a)$

reactant[a]	$n_{\alpha\text{-H}}$	k'_{enolate}[e] (ks-kPa-(Ti–O))$^{-1}$	$\Delta G'^{\ddagger}_{\text{enolate}}$[f] (kJ mol^{-1})	$k_{CO}K_{ol}K_H$ $(k_{CC}K_{al})^{-1}$	$\Delta\Delta G^{\ddagger}_{\text{ester-aldol}}$[g] (kJ mol^{-1})
$C^{\#}H_3CHO$[b]	3	37.7 ± 0.4	125 ± 1	0.034 ± 0.001	15 ± 1
$C^{\#}D_3CDO$[b]	3	15.9 ± 0.1	129 ± 1	0.025 ± 0.001	16 ± 1
$CH_3C^{\#}H_2CHO$[c]	2	31.3 ± 0.9	126 ± 1	0.101 ± 0.003	10 ± 1
$CH_3CH_2C^{\#}H_2CHO$[c]	2	20.6 ± 0.4	127 ± 1	0.152 ± 0.002	8 ± 1
$CH_3(CH_2)_2C^{\#}H_2CHO$[c]	2	17.8 ± 0.4	128 ± 1	0.194 ± 0.004	7 ± 1
$(CH_3)_2CHC^{\#}H_2CHO$[c]	2	0.64 ± 0.01	143 ± 1	2.36 ± 0.02	−4 ± 1
$CH_3COC^{\#}H_3$[d]	6	4.80 ± 0.05	134 ± 1	[h]	[h]
$CH_3CH_2COC^{\#}H_3$[d]	3	2.55 ± 0.03	137 ± 1	[h]	[h]
$CH_3C^{\#}H_2COCH_3$[d]	2	1.11 ± 0.02	140 ± 1	[h]	[h]

[a] α-C atoms from which a H atom is abstracted in the formation of the enolate are indicated by the pound sign (#). [b] Data shown in Figure 2. [c] Data shown in Figure 3. [d] Data shown in Figure 4. [e] Normalized by $n_{\alpha\text{-H}}$. [f] Calculated from eq 7. [g] Calculated from eq 9. [h] Esterification reactions cannot occur from alkanones and nonterminal alkanols, because dehydrogenation to form an ester from hemiacetal intermediates (formed from alkanones) cannot occur at an OH group bound to a tertiary C atom.

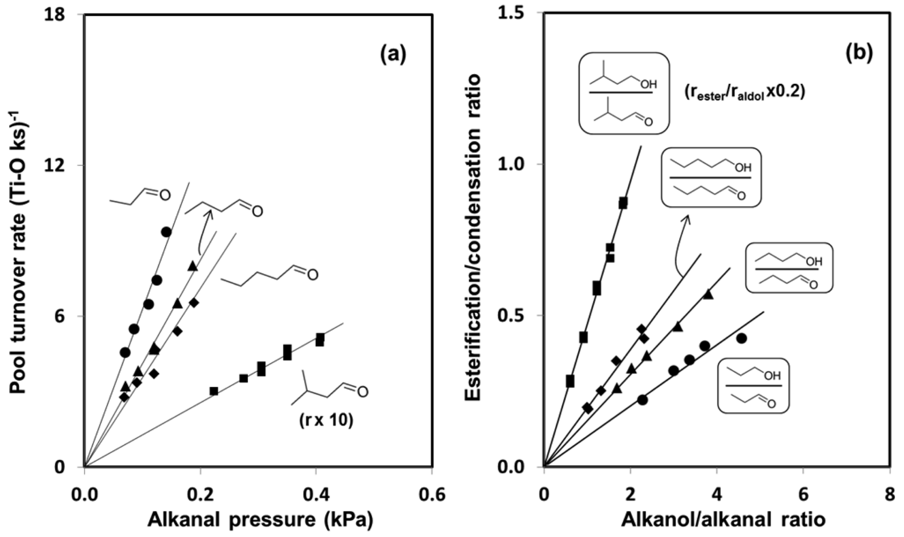

Figure 3. Effects of (a) alkanal pressure in equilibrated alkanol–alkanal reactants on pool turnover rates and (b) alkanol/alkanal ratio on ratios of esterification and condensation rates ($TiO_2(a)$ + 20% wt Cu/SiO_2 (1:1 mass), 523 K, 0.8 kPa alkanol, 10–60 kPa H_2). Solid lines in a and b represent the regression fits to the functional forms of eqs 5 and 6, respectively. Data for 1-propanol–propanal mixtures have been adapted from ref 30.

and stabilization of the enolate moiety (by metal centers). The $k_{CO}K_{ol}K_H$ $(k_{CC}K_{al})^{-1}$ term in eq 6 corresponds to the slope of the selectivity ratios in Figure 2b; it accounts for the relative rates of C–O coupling (step 10, Scheme 3) and C–C coupling (step 4, Scheme 3) steps from a given enolate intermediate.

Deuterated C_2D_5OD–CD_3CDO–D_2 mixtures were also fully equilibrated on $TiO_2(a)$ + Cu/SiO_2 mixtures (1:1 mass) at all conditions (η_{dehy} 0.9–1; Figure S1, Supporting Information (SI)); their conversion rates were proportional to alkanal pressure (Figure 2a), but the rate constants were smaller than for undeuterated reactants ($(k'_{\text{enolate}})_H/(k'_{\text{enolate}})_D$ = 2.3; 523 K; Table 1). These normal kinetic isotope effects are consistent with kinetically relevant α-C–H bond cleavage steps. These values are similar to those derived from DFT treatments for the formation of enolates from ethanal (2.4; section 3.5) and also to those measured (2.4; 523 K) and calculated (2.5; 523 K) for enolate formation from acetone.[30]

Deuterated ethanol–ethanal mixtures gave esterification/condensation rate ratios only slightly smaller than for undeuterated reactants ($(k_{CO}K_{ol}K_H\ (k_{CC}K_{al})^{-1})_H/(k_{CO}K_{ol}K_H\ (k_{CC}K_{al})^{-1})_D$ = 1.4; 523 K; Table 1), indicating that the kinetically relevant steps for both condensation and esterification reactions from enolates involve either similar hydrogen rearrangements or none at all. DFT treatments (section 3.5) show that the condensation steps from enolates are limited by the C–C bond formation in enolate–alkanal pairs (step 4, Scheme 3); esterification, in contrast, is limited by C–O bond formation in alkanal–alkoxide pairs (step 10, Scheme 3) after fast and equilibrated transfer of a H atom in enolate–alkanol pairs (step 9, Scheme 3). The limiting steps in either C–C and C–O coupling reactions do not involve activation of H atoms; indeed, DFT treatments predict weak H/D isotope effects on esterification/condensation rate ratios (1.2; 523 K; section 3.5), consistent with measured values (1.4; Table 1).

Hydrogenation–dehydrogenation equilibria for C_3–C_5 alkanol reactants (i.e., 1-propanol, 2-propanol, 1-butanol, 2-butanol, 1-pentanol, and 3-methyl-1-butanol) were also achieved (η_{dehy} 0.9–1.0) on $TiO_2(a)$ + Cu/SiO_2 mixtures (1:1 mass; 523 K, 10–60 kPa H_2). These equilibrated 1-alkanol–alkanal and 2-alkanol–alkanone reactant pools formed the products expected from their aldol condensation and esterification reactions (Scheme 2). Equilibrated mixtures of alkanones and their nonterminal alkanol hydrogenation products cannot form esters because –OH groups at tertiary C atoms in hemiacetal intermediates formed (step 12, Scheme 3) cannot dehydrogenate to their more stable ester analogs (step 13, Scheme 3). Butanone can form two condensation products, depending on the location of α-H atom abstracted. Abstraction at the primary C atom ($CH_3CH_2COC^{\#}H_3$) forms 5-methyl-3-heptanone, while activation at the secondary C atom ($CH_3C^{\#}H_2COCH_3$) forms 3,4-dimethyl-2-hexanone.

The effects of carbonyl reactant pressure and of alkanol/alkanal ratios on rates and esterification/condensation rate ratios obey eqs 5 and 6, respectively, for all reactants (Figures 3 and 4; Table 1). The mechanistic conclusions reached for ethanol−ethanal reactants above and for C_3 oxygenates elsewhere[30] seem general and accurately account for the formation rate and conversion selectivity of enolates on $TiO_2(a)$ and, without any required modifications, also on $ZrO_2(m)$ (section 3.2).

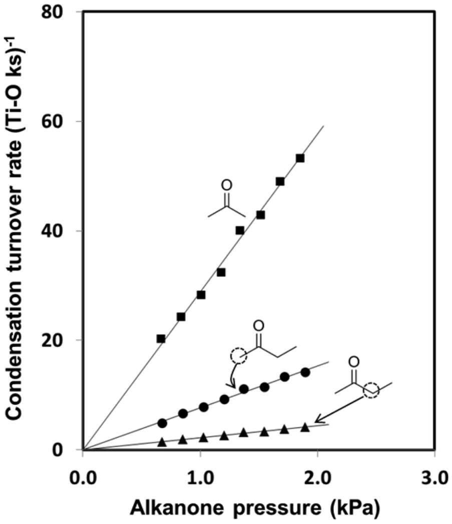

Figure 4. Effects of alkanone pressure in equilibrated 2-alkanol−alkanone reactants on condensation turnover rates ($TiO_2(a)$ + 20% wt Cu/SiO_2 (1:1 mass), 523 K, 0.8−2.0 kPa 2-alkanol, 40 kPa H_2). Solid lines represent the regression fits to the functional form of eq 5. Data for 2-propanol−acetone mixtures have been adapted from ref 30.

For all reactant mixtures, the k'_{enolate} term in eq 5 reflects the free Gibbs energy barrier ($\Delta G'^{\ddagger}_{\text{enolate}}$) to form the enolate transition state (TS) from a gaseous alkanal (alkanone) molecule and a bare acid−base site pair ($TiO_2(a)$ used in Scheme 4 as the illustrative example)

$$k'_{\text{enolate}} = \frac{k_B T}{h}\exp\left(-\frac{\Delta G'^{\ddagger}_{\text{enolate}}}{RT}\right) \tag{7}$$

$$\Delta G'^{\ddagger}_{\text{enolate}} = G^{\ddagger}_{\text{enolate}} - G_{\text{carbonyl}} - G_{\text{Ti-O}} \tag{8}$$

where $G^{\ddagger}_{\text{enolate}}$, G_{carbonyl}, and $G_{\text{Ti-O}}$ are the Gibbs free energies for the enolate formation TS, the gaseous carbonyl reactant (i.e., alkanal or alkanone), and the bare Ti−O pair. The $\Delta G'^{\ddagger}_{\text{enolate}}$ (523 K) values derived from measured k'_{enolate} increased slightly but systematically from 125 ± 1 (ethanal) to 128 ± 1 kJ mol^{-1} (pentanal) as the alkyl chains bound to the C=O group lengthened (Table 1). The slightly lower reactivity of alkanals with longer chains predominantly reflects steric effects at the α-C atom, because DFT-derived α-C−H bond heterolytic dissociation energies are actually lower for alkanals with longer alkyl chains (from 1565 to 1545 kJ mol^{-1}; section 3.6). Measured $\Delta G'^{\ddagger}_{\text{enolate}}$ values were much larger for branched 3-methyl-butanal (143 ± 1 kJ mol^{-1}; Table 1) than for linear C_2−C_5 alkanals (125−128 kJ mol^{-1}; Table 1), consistent with steric effects by bulkier substituents at the α-C atom and with the DFT-derived barriers for enolate formation steps (section 3.5).

C_3 and C_4 alkanones showed larger $\Delta G'^{\ddagger}_{\text{enolate}}$ values than linear C_2−C_5 alkanals, indicating that alkyls at carbonyl C atoms also interfere with enolate formation, in this case,

Scheme 4. Schematic Reaction Coordinate Diagram for Enolate Formation from a Gaseous Alkanal (alkanone) Reactant on a Ti−O Site Pair of $TiO_2(a)$[a]

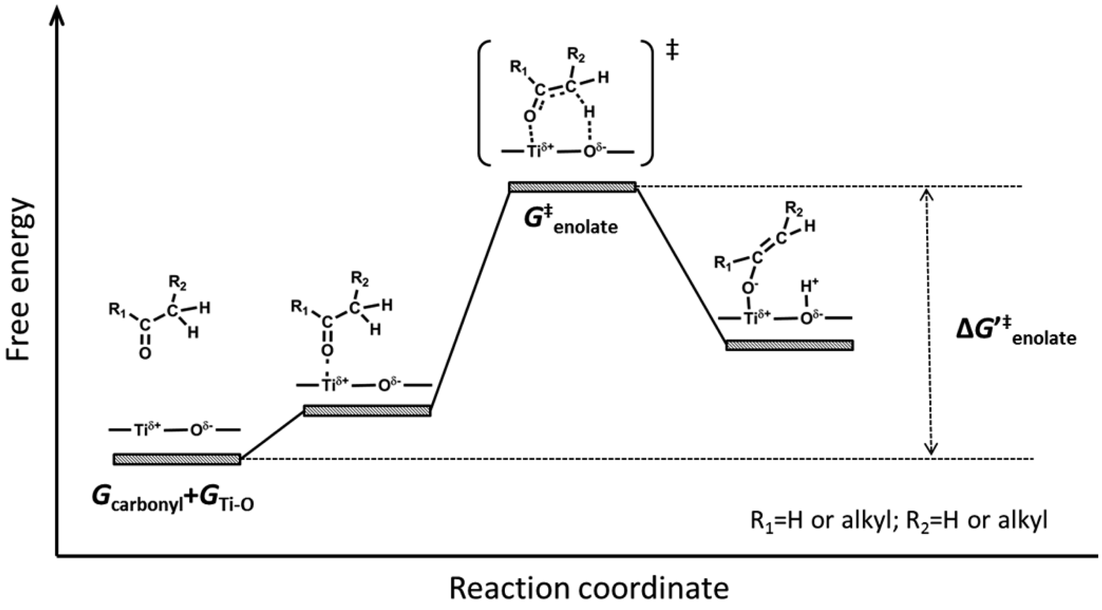

[a] $\Delta G'^{\ddagger}_{\text{enolate}}$ represents the experimentally-measurable free energy barrier of the enolate formation (eq 7).

Scheme 5. Schematic Reaction Coordinate Diagram for the Formation of C−C and C−O Bonds from Alkanal-Derived Enolates with Alkanal or Alkanol Reactants on Ti−O−Ti Surface Structures of $TiO_2(a)$[a]

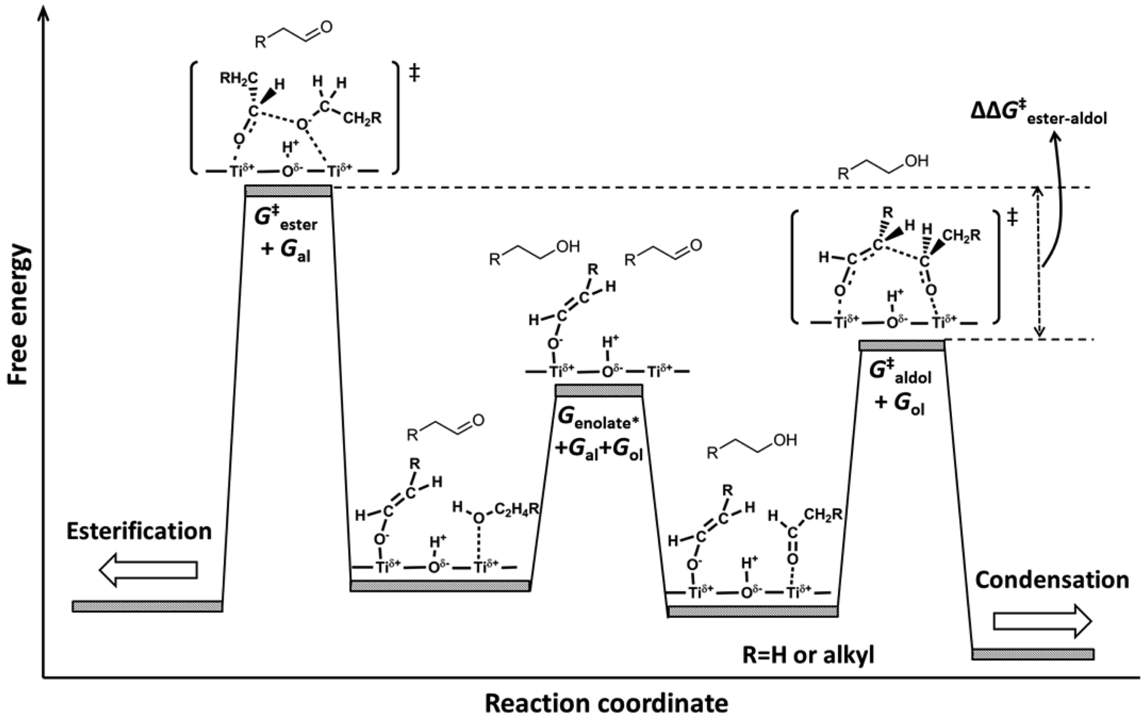

[a] $\Delta\Delta G^‡_{\text{ester-aldol}}$ represents the experimentally-accessible difference in free energy barriers for esterification and aldol condensation (eq 9).

because of the combined effects of steric hindrance and of electronic effects on the strength of the C−H bonds at the α position, as shown by theoretical treatments in section 3.6. The replacement of the H atom at the α-C atom with a $-CH_3$ group influenced $\Delta G'^‡_{\text{enolate}}$ for acetone (vs butanone) more strongly than for ethanal (vs propanal) (6 ± 2 vs 1 ± 2 kJ mol^{-1}; Table 1). DFT treatments (section 3.6) confirmed that $-CH_3$ groups at the α-C atom in alkanones distort enolate formation transition states much more significantly than in alkanals.

The ratio of rate constants for C−O and C−C formation from enolates ($k_{CO}K_{ol}K_H$ $(k_{CC}K_{al})^{-1}$) reflects differences in the free energy barriers ($\Delta\Delta G^‡_{\text{ester-aldol}}$; Scheme 5) between C−O coupling (step 10, Scheme 3) and C−C coupling (step 4, Scheme 3) steps

$$\frac{k_{CO}K_{ol}K_H}{k_{CC}K_{al}} = \exp\left(-\frac{\Delta\Delta G^‡_{\text{ester-aldol}}}{RT}\right) = \exp\left(-\frac{\Delta G^‡_{\text{ester}} - \Delta G^‡_{\text{aldol}}}{RT}\right) \tag{9}$$

$$\Delta G^‡_{\text{ester}} = G^‡_{\text{ester}} - G_{ol} - G_{\text{enolate}*} \tag{10}$$

$$\Delta G^‡_{\text{aldol}} = G^‡_{\text{aldol}} - G_{al} - G_{\text{enolate}*} \tag{11}$$

$$\Delta\Delta G^‡_{\text{ester-aldol}} = G^‡_{\text{ester}} - G^‡_{\text{aldol}} + G_{al} - G_{ol} \tag{12}$$

$\Delta G^‡_{\text{ester}}$ is the free energy difference between the C−O coupling TS ($G^‡_{\text{ester}}$) and the sum of a gaseous alkanol reactant (G_{ol}) and an enolate bound on a T−O site pair ($G_{\text{enolate}*}$) (eq 10; Scheme 5); $\Delta G^‡_{\text{aldol}}$ represents the free energy difference between the C−C coupling TS ($G^‡_{\text{aldol}}$) and the sum of a gaseous alkanal reactant (G_{al}) and an enolate bound on a T−O site pair ($G_{\text{enolate}*}$) (eq 11; Scheme 5).

Measured $\Delta\Delta G^‡_{\text{ester-aldol}}$ values decreased from 15 ± 1 (ethanol−ethanal) to 7 ± 1 kJ mol^{-1} (1-pentanol−pentanal) (523 K; Table 1) as alkyl chains lengthened, because larger alkyl chains destabilize the C−C coupling TS more strongly than the C−O coupling TS relative to their respective gaseous reactants. Consistent with this trend for linear alkanals, 3-methyl-butanal, with an isopropyl chain at the α-C atom, actually favors esterification turnovers ($\Delta\Delta G'^‡_{\text{ester-aldol}} = -4 \pm 1$ kJ mol^{-1}; Table 1) because of its bulkier substituent. DFT treatments show that alkyl groups in enolate−alkanal pairs at the C−C coupling TS are much closer to each other than in alkoxide−alkanal pairs at the C−O coupling TS (shown in section 3.8); this leads to stronger steric effects for C−C coupling than C−O coupling transition states and thus to smaller $\Delta\Delta G^‡_{\text{ester-aldol}}$ values for longer alkanal/1-alkanol reactants.

These data show that α-C−H bond cleavage to form enolates is the sole kinetically relevant step in reactions of C_2−C_5 oxygenates on $TiO_2(a)$, as also found on $ZrO_2(m)$ (section 3.2). In contrast, esterification/condensation rate ratios are mediated by C−O and C−C coupling reactions of enolates with alkanol and carbonyl coadsorbed reactants, respectively. The acid−base site pairs exposed at $TiO_2(a)$ and $ZrO_2(m)$ surfaces stabilize the enolate formation TS as well as those that mediate subsequent C−O and C−C coupling reactions. Stabilization requires concerted interactions with acid−base site pairs of intermediate strength (section 3.2). Rates and selectivities are also influenced by the structure of the reactant molecules. For example, alkyl groups influence alkanal reactivity through steric effects that compensate for the weakening of the more substituted α-C−H bonds, while steric hindrance and α-

C−H bond strength combine to make alkanones significantly less reactive than the respective alkanals with similar alkyl chains at the α-C atom. The C−C coupling TS involves coreactants in tighter configurations than the C−O coupling TS; as a result, esterification rates are less inhibited by alkyl chains than condensation rates.

The above conclusions, derived here from experiments using reactant pools formed from a single alkanol, alkanal, or alkanone, are confirmed in section 3.3 using mixtures of C_2−C_4 reactants. These reactions also provide kinetic details about the reactivity of enolates with alkanols and alkanals/alkanones derived from a different carbonyl precursor. Such kinetic details cannot be extracted from reactant streams consisting solely of one alkanol or its equilibrated carbonyl analog.

3.2. Site Titrations, Turnover Rates, and Selectivities on Monoclinic ZrO_2 Surfaces.

$ZrO_2(m)$ also catalyzes aldol condensation and esterification reactions of alkanol and carbonyl reactants.[21−23] Acid−base properties of $ZrO_2(m)$ surfaces were examined here using site titrations with CO_2, pyridine, and propanoic acid during acetone condensation on $ZrO_2(m)$ + Cu/SiO_2 mixtures (523 K; 4 kPa acetone; 40 kPa H_2).

Condensation rates on $ZrO_2(m)$ + Cu/SiO_2 mixtures (1:1 mass) decreased from 4.9 to 2.3 μmol C atom m^{-2} s^{-1} when CO_2 (4 kPa) was introduced into the acetone reactant stream (CO_2/acetone = 1.0; Figure 5); rates recovered gradually upon CO_2 removal (ca. 3 h, section S2, SI), suggesting that relatively weak basic sites[16] are involved in condensation turnovers. These basic sites are stronger than on $TiO_2(a)$, for which condensation rates were unaffected by 4 kPa CO_2.[30] Pyridine (200 Pa; pyridine/acetone = 0.05) did not affect acetone condensation rates on $ZrO_2(m)$ (Figure 5), indicating that strong Brønsted or Lewis acid sites[15] are not present or required for enolate formation. Lewis acid−base site pairs account for enolate formation on $TiO_2(a)$, for which pyridine, even at lower pressures (20 Pa; pyridine/acetone = 0.005), led to small but detectable (and reversible) rate changes (ca. 20%; 523 K, 4 kPa acetone, 40 kPa H_2). These data seem to indicate that Zr centers on $ZrO_2(m)$ surfaces are involved in condensation turnovers; such Zr centers are, however, weaker Lewis acids than Ti centers in $TiO_2(a)$, while O atoms on $ZrO_2(m)$ are stronger basic sites than those on $TiO_2(a)$.

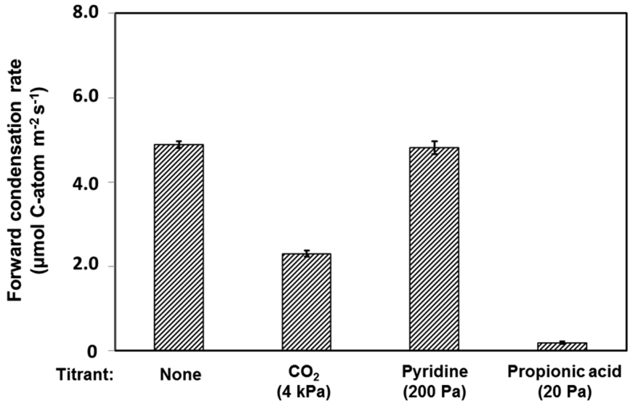

Figure 5. Effects of CO_2, pyridine, and propanoic acid introductions on areal forward acetone condensation rates ($ZrO_2(m)$ + 20% wt Cu/SiO_2 (1:1 mass), 523 K, 4 kPa acetone, 4 kPa CO_2, 200 Pa pyridine, 20 Pa propanoic acid, 40 kPa H_2).

Propanoic acid binds onto Zr−O pairs to form carboxylate species bound at two adjacent Zr centers with the H atom from its OH group bound at a lattice O atom; such surfaces saturate at an acid/Zr stoichiometry of 0.5, as shown by infrared spectra[34] and DFT treatments.[33] The presence of propanoic acid (20 Pa; acid/acetone = 0.005) led to strong suppression of acetone condensation rates (from 4.9 to 0.2 μmol C atom m^{-2} s^{-1}; Figure 5); rates recovered only very gradually over an extended period of time (ca. 5 h; section S2, SI); these data confirm the presence of Zr−O pairs of moderate acid−base strength and their involvement in condensation turnovers. They also show that O atoms appear to act as a stronger base (based on CO_2 effects) and Zr centers as weaker Lewis acids (based on pyridine effects) than Ti−O species in $TiO_2(a)$ but that both surfaces can strongly bind carboxylic acids in dissociated forms using acid−base site pairs present on these surfaces.[30,33]

Titrations during acetone condensation at lower temperatures (443 K) led to irreversible adsorption of propanoic acid and to the full suppression of condensation rates on $ZrO_2(m)$, thus allowing the measurement of the number of accessible Zr−O site pairs from the number of adsorbed propanoic acid molecules requited to suppress rates. These Zr−O surface densities (6.0 nm^{-2}, Figure 6) resemble those estimated from crystallography for low-index $ZrO_2(m)$ surfaces (6.8 (-111), 8.1 (111), and 5.7 nm^{-2} (-101); monoclinic ZrO_2, space group $P2_1/c$, a = 0.515 nm, b = 0.521 nm, c = 0.532 nm).[60] Such site densities, taken together with those measured by similar methods for Ti−O site pairs on $TiO_2(a)$ (3.7 nm^{-2}),[30] allow, for the first time, a rigorous comparison of reactivity as turnover rates for $ZrO_2(m)$ and $TiO_2(a)$ surfaces and accurate theory−experiment benchmarking.

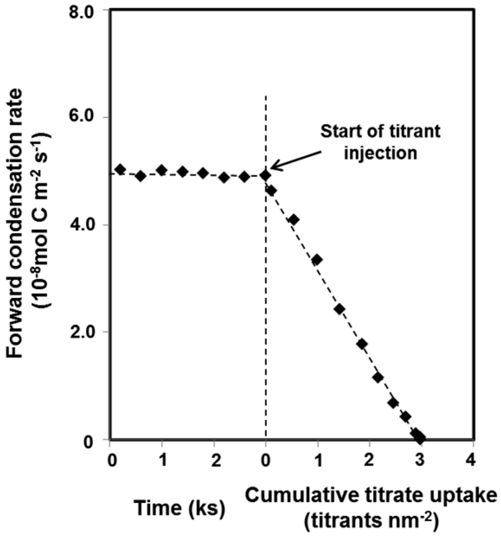

Figure 6. Forward acetone condensation rates before (vs time) and after (vs cumulative titrant uptake) propanoic acid introduction ($ZrO_2(m)$ + 20% wt Cu/SiO_2 (1:1 mass), 443 K, 0.8 kPa acetone, 20 Pa propanoic acid, 20 kPa H_2). Dashed lines are linear regression fits.

As in the case of $TiO_2(a)$ (section 3.1), ethanol−ethanal interconversions were equilibrated on $ZrO_2(m)$ + Cu/SiO_2 mixtures (1:1 mass; 523 K; 15−40 kPa H_2; η_{dehy} 0.9−1); the lumped ethanol−ethanal reactants formed the expected condensation and esterification products (Scheme 2). Turnover rates were proportional to ethanal pressure (Figure 7a; eq 5)

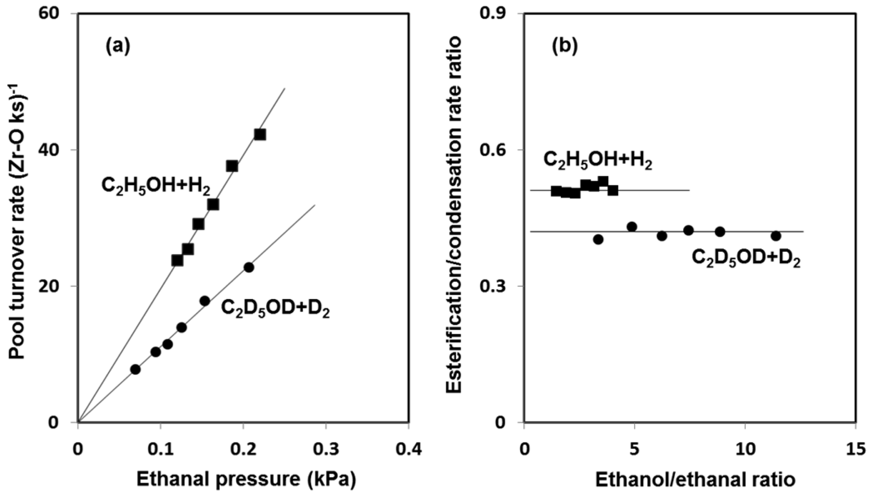

Figure 7. Effects of (a) ethanal pressure on pool turnover rates and of (b) ethanol/ethanal ratio on ratios of esterification and condensation rates ($ZrO_2(m)$ + 20% wt Cu/SiO_2 (1:1 mass), 523 K, 0.6 kPa ethanol or 1.0 kPa ethanol-d_6, 15−40 kPa H_2/D_2). Solid lines in a and b represent the regression fits to the functional forms of eqs 14 and 22, respectively.

Table 2. Number of α-H Atoms ($n_{\alpha\text{-H}}$) and Measured $k'_{\text{enolate,total}}$ and $k'_{\text{enolate,B}}(k'_{\text{enolate,A}})^{-1}$ Values for Enolate Formation and for Esterification and Condensation Reactions, Respectively, of Ethanal and Acetone Reactants on $ZrO_2(m)$

reactant[a]	$n_{\alpha\text{-H}}$	$k'_{\text{enolate,total}}$[d] (ks-kPa-(Zr−O))$^{-1}$	$k'_{\text{enolate,B}}(k'_{\text{enolate,A}})^{-1}$
$C^{\#}H_3CHO$[b]	3	65.4 ± 0.6	0.51 ± 0.01
$C^{\#}D_3CDO$[b]	3	37.1 ± 0.5	0.41 ± 0.01
$C^{\#}H_3COCH_3$[c]	6	6.70 ± 0.05	[e]
$C^{\#}D_3COCD_3$[c]	6	2.61 ± 0.03	[e]

[a] α-C atoms from which a H atom is abstracted in the formation of the enolate are indicated by the pound sign ($^{\#}$). [b] Data shown in Figure 7. [c] Data shown in section S3, SI. [d] Normalized by $n_{\alpha\text{-H}}$. [e] Esterification reactions cannot occur from 2-propanol−acetone reactants, because dehydrogenation to form an ester from hemiacetal intermediates (formed from alkanones) cannot occur at an OH group bound to a tertiary C atom.

Scheme 6. Exposed Zr and O Centers for a Unit Cell of Monoclinic ZrO_2 (−111) Surfaces[a]

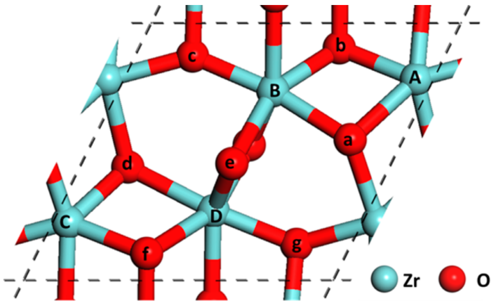

Zr	E_{HA} (kJ mol^{-1})	O	E_{PA} (kJ mol^{-1})
A	-53	a	-1562
B	-8	b	-1461
C	-27	c	-1560
D	< -1	d	< -1461
		e	-1619
		f	-1522
		g	-1543

[a] DFT-derived affinities of these Zr and O centers for OH^- (E_{HA}, eq 1) or H^+ (E_{PA}, eq 2) gaseous species are included.

and showed normal H/D isotope effects ($(k'_{\text{enolate}})_H/(k'_{\text{enolate}})_D$ = 1.8; 523 K; Table 2), similar to those on $TiO_2(a)$ (2.3; Table 1) and consistent with the kinetically relevant formation of enolates via α-C−H bond activation in ethanal on surfaces sparsely covered with intermediates. These first-order kinetic dependence and normal H/D isotope effects were also observed for acetone condensation on $ZrO_2(m)$ (Table 2; data shown in section S3, SI). Measured k'_{enolate} values (per site pair) for ethanal and acetone are both slightly higher on $ZrO_2(m)$ than on TiO_2 (ethanal, 65.4 vs 37.7 (ks-kPa-(M−O))$^{-1}$; acetone, 6.70 vs 4.80 (ks-kPa-(M−O))$^{-1}$; Tables 1 and 2). These data indicate that acid−base site pairs on $ZrO_2(m)$ are slightly more effective than on $TiO_2(a)$ in α-C−H bond activation for both reactants. The higher reactivity of $ZrO_2(m)$ surfaces reflects their more strongly basic lattice O atoms, which compensate for the weaker acid centers in the stabilization of the concerted enolate formation TS.

$ZrO_2(m)$ (+Cu/SiO_2) gave esterification/condensation rate ratios that did not depend on ethanol/ethanal ratios (Figure 7b), in sharp contrast with the proportional effects observed on $TiO_2(a)$ (Figure 2b). These different trends appear to reflect the presence of more than one type of active structures on $ZrO_2(m)$ surfaces ($ZrO_2(m)$ (−111) surface used here as the illustrative example; Scheme 6) instead of different kinetically relevant steps for condensation and esterification routes of bound enolates (Scheme 3). The most stable and typically exposed $ZrO_2(m)$ (−111) surface has four distinct Zr centers and seven types of O centers; they are distinct because of the number and distance of the nearest counterions.[51] The DFT-derived OH^- affinities (E_{HA}, eq 1) of the Zr centers ranged

Scheme 7. C−C and C−O Coupling Transition State Structures for Enolates Bound on the Zr$_A$ Site of the Zr$_A$−O−Zr$_B$ Surface Structure[a]

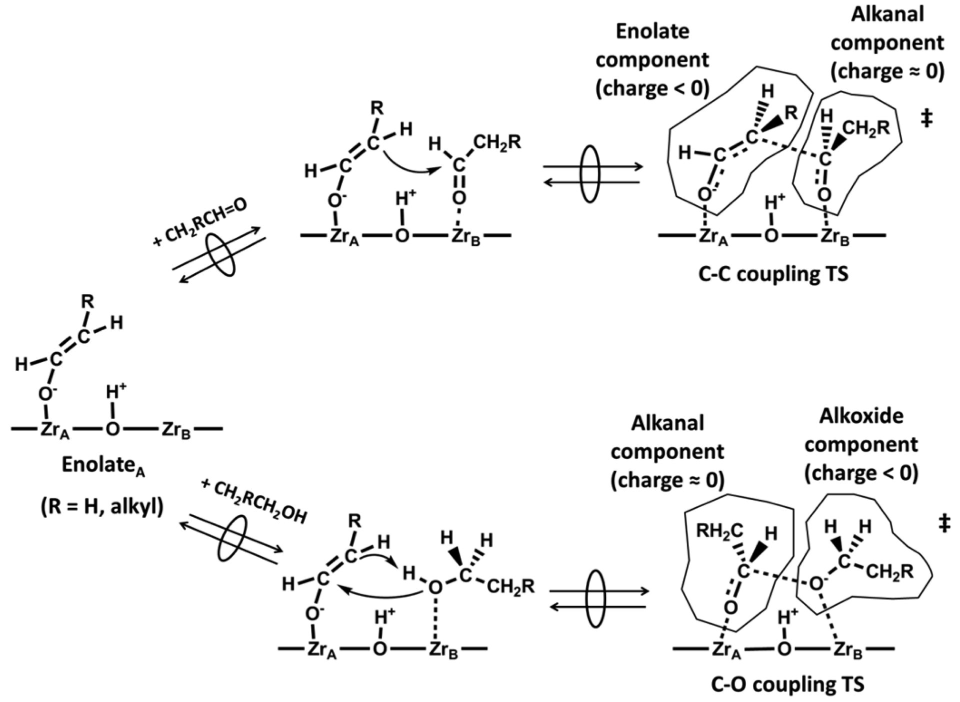

[a] Enolate$_A$ with respective alkanal and 1-alkanol coreactants. The enolate formation transition states on Zr$_B$ are the same but with the other species on Zr$_A$.

from −1 to −54 kJ mol^{-1} (Scheme 6); the respective H$^+$ affinities of the O centers (E_{PA}, eq 2) ranged from −1461 to −1619 kJ mol^{-1} (Scheme 6). These different affinities lead to an expectation that the reactivity of these diverse structures would also differ significantly.

One of the Zr−O pairs in Zr−O−Zr structures converts an alkanal to an enolate via cleavage of the α-C−H bond in the carbonyl reactant (steps 1 and 2, Scheme 3), while the other Zr center in Zr−O−Zr structures must then bind the coreactant required for C−C or C−O coupling steps (steps 3−6 or 8−12, Scheme 3). Here, Zr$_A$−O−Zr$_B$ sites (shown in Scheme 6) are used to illustrate how the asymmetric nature of Zr−O−Zr structures can affect their reactivity for enolate formation and the extent to which enolates convert to esterification or condensation products. Enolate formation from alkanals can occur on either Zr$_A$−O or Zr$_B$−O site pairs at asymmetric Zr$_A$−O−Zr$_B$ structures at rates with similar functional forms

$$\frac{r_{\text{enolate},i}}{[L]} = k'_{\text{enolate},i}P_{\text{alkanal}} \tag{13}$$

but different rate constants ($k'_{\text{enolate},i}$; i = A, B); their combined contributions then give the total enolate formation rates

$$\frac{r_{\text{enolate,total}}}{[L]} = (k'_{\text{enolate,A}} + k'_{\text{enolate,B}})P_{\text{alkanal}} = k'_{\text{enolate,total}}P_{\text{alkanal}} \tag{14}$$

which preserves the first-order nature of measured rates with an effective kinetic constant of $k'_{\text{enolate,total}}$, in agreement with experiments (Figure 7a).

The enolate bound at Zr$_A$ (Enolate$_A$) can then nucleophilically attack a coadsorbed alkanal or 1-alkanol at Zr$_B$ to form C−C and C−O bonds, respectively (Scheme 3). Conversely, enolates formed at Zr$_B$ (Enolate$_B$) can attack species coadsorbed at Zr$_A$. We assume, by analogy with TiO$_2$(a) (eq 6), that the ratios of esterification ($r_{\text{ester,i}}$) to condensation ($r_{\text{aldol,i}}$) for each enolate$_i$ (i = A, B) are given by

$$\frac{r_{\text{ester},i}}{r_{\text{aldol},i}} = \frac{\alpha_i P_{\text{alkanol}}}{P_{\text{alkanal}}} \tag{15}$$

in which α_i is the $k_{\text{CO}}K_{\text{ol}}K_{\text{H}}$ $(k_{\text{CC}}K_{\text{al}})^{-1}$ term for the C−O and C−C coupling reactions of enolates bound on Zr$_i$ (i = A, B) and the sum of $r_{\text{ester},i}$ and $r_{\text{aldol},i}$ is equal to $r_{\text{enolate},i}$

$$r_{\text{enolate},i} = r_{\text{ester},i} + r_{\text{aldol},i} \tag{16}$$

These equations (eqs 13, 15, and 16) can then be used to describe measured esterification and condensation rates ($r_{\text{ester,total}}$; $r_{\text{aldol,total}}$) and their rate ratios ($r_{\text{ester,total}}/r_{\text{aldol,total}}$) for Zr$_A$−O−Zr$_B$ surface structures (derivation in section S4, SI)

$$\frac{r_{\text{ester,total}}}{[L]} = \sum_{i\in\{\text{A,B}\}} \frac{\alpha_i k'_{\text{enolate},i}P_{\text{alkanol}}P_{\text{alkanal}}}{\alpha_i P_{\text{alkanol}} + P_{\text{alkanal}}} \tag{17}$$

$$\frac{r_{\text{aldol,total}}}{[L]} = \sum_{i\in\{\text{A,B}\}} \frac{k'_{\text{enolate},i}(P_{\text{alkanal}})^2}{\alpha_i P_{\text{alkanol}} + P_{\text{alkanal}}} \tag{18}$$

$$\frac{r_{\text{ester,total}}}{r_{\text{aldol,total}}} = \frac{\sum_{i\in\{\text{A,B}\}} \frac{\alpha_i k'_{\text{enolate},i}P_{\text{alkanol}}}{\alpha_i P_{\text{alkanol}} + P_{\text{alkanal}}}}{\sum_{i\in\{\text{A,B}\}} \frac{k'_{\text{enolate},i}P_{\text{alkanal}}}{\alpha_i P_{\text{alkanol}} + P_{\text{alkanal}}}} \tag{19}$$

As a result, measured esterification/condensation rate ratios (eq 19) depend linearly on alkanol/alkanal ratios when α_A and α_B have similar values but become independent of these ratios when the magnitudes of α_A and α_B differ significantly.

Scheme 8. Aldol Condensation between (a) Ethanal and Propanal and between (b) Acetone and Propanal on Bifunctional TiO_2 + Cu/SiO_2 Catalysts

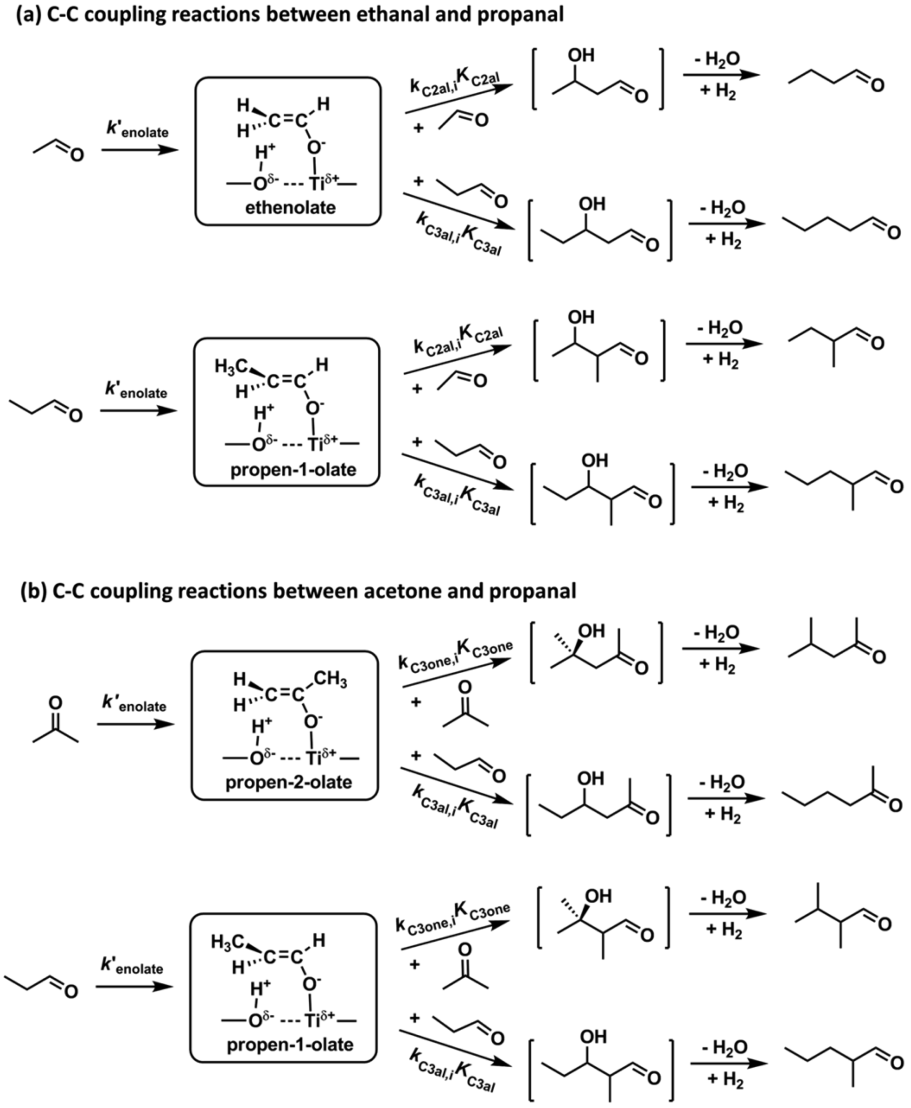

As for the condensation and esterification selectivities of an enolate bound on a Ti center (eqs 9–12; Scheme 5), each α_i term (i = A, B) in eq 15 reflects the difference ($\Delta\Delta G^{\ddagger}_{\text{ester},i\text{-aldol},i}$) between free energies of the enolate–alkanal C–C coupling and the alkanal–alkoxide C–O coupling transition states derived from an enolate bound to a Zr_i site ($G^{\ddagger}_{\text{aldol},i}$, $G^{\ddagger}_{\text{ester},i}$; referenced to a bare Zr_A–O–Zr_B surface structure and respective gaseous reactants for each step)

$$\alpha_i = \exp\left(-\frac{\Delta\Delta G^{\ddagger}_{\text{ester},i-\text{aldol},i}}{RT}\right) \tag{20}$$

$$\Delta\Delta G^{\ddagger}_{\text{ester},i-\text{aldol},i} = G^{\ddagger}_{\text{ester},i} - G^{\ddagger}_{\text{aldol},i} + G_{\text{al}} - G_{\text{ol}} \tag{21}$$

Here G_{al} and G_{ol} are free energies of gaseous alkanal and alkanol reactants, respectively. Equation 20 shows that these α_i terms (i = A, B) depend most sensitively on how differently Zr_A and Zr_B interact with C–C and C–O coupling transition states.

In C–C coupling, the enolate and the alkanal bind at Zr_A–O–Zr_B structures with their respective O atoms interacting with one Zr center at the TS (Scheme 7). The C–C coupling TS contains a slightly anionic enolate (−0.20; section S12, SI) and a nearly neutral alkanal (−0.02; section S12, SI), thus making the strength of the Lewis acid more consequential for enolate than alkanal stability. The C–C coupling TS is more stable when the enolate binds on Zr_A, which shows the stronger OH^- affinity (Scheme 6).

The O atoms in the alkanal and alkoxide moieties at the C–O coupling TS also interact with each of the two Lewis acid centers in Zr_A–O–Zr_B structures (Scheme 7). At the TS, the alkoxide is slightly anionic (−0.31; section S12, SI) and the alkanal is nearly neutral (0.03; section S12, SI). The C–O coupling TS is therefore more stable when the alkoxide (formed from 1-alkanol) binds on Zr_A, the site with the stronger OH^- affinity in Zr_A–O–Zr_B structures (Scheme 6). Consequently, esterification is favored over condensation when the enolate precursor that forms the alkanal (via H transfer from the alkanol; Scheme 7) binds at the weaker Zr center. The strong preference for C–C or C–O coupling transition states when the enolate binds to Zr_A or Zr_B and the consequently smaller values of α_A than α_B reflect the very different OH^-

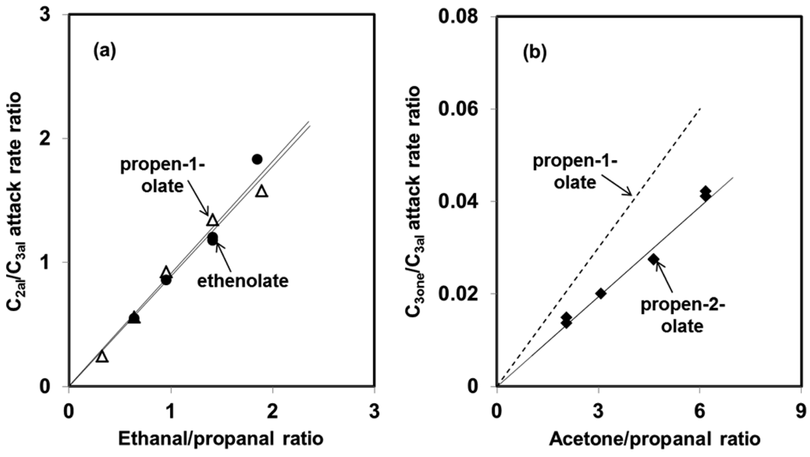

Figure 8. Effects of reactant pressure ratio on ratios of C−C coupling rates for (a) ethanal−propanal and (b) acetone−propanal reactants ($TiO_2(a)$ + 20% wt Cu/SiO_2 (1:1 mass), 523 K, 0−2.0 kPa ethanol/acetone, 0.5 kPa 1-propanol, 20 kPa H_2). Solid lines in a and b represent regression fits to the functional form of eq 23. Dashed line in b represents the maximum rate ratios estimated using the detection limit of the flame ionization detector.

affinities of the Zr_A or Zr_B centers in $Zr_A{-}O{-}Zr_B$ structures at $ZrO_2(m)$ surfaces (−53 vs −8 kJ mol^{-1}; Scheme 6).

These very different values of α_i ($\alpha_A < \alpha_B$) allow eq 19 to be simplified to

$$\frac{r_{\text{ester,total}}}{r_{\text{aldol,total}}} = \frac{k'_{\text{enolate,B}}}{k'_{\text{enolate,A}}} \tag{22}$$

These ratios do not depend on alkanol/alkanal ratios, in accordance with measurements (Figure 7b). They reflect the ratio of enolate formation rate constants at Zr_B and Zr_A sites ($k'_{\text{enolate,B}}/k'_{\text{enolate,A}}$), which depends, in turn, on the relative stability of the enolate formation TS on $Zr_B{-}O$ and $Zr_A{-}O$ pairs. On $TiO_2(a)$, the two Ti centers at Ti−O−Ti surface structures are crystallographically and chemically identical, leading to ratios of esterification and condensation rates that depend on the concentrations of the C−O and C−C coupling transition states (eq 6); these ratios reflect the relative stability of the C−O and C−C coupling transition states and the concentrations of their respective alkanol and alkanal coreactants that react with the enolate on $TiO_2(a)$.

These $k'_{\text{enolate,B}}/k'_{\text{enolate,A}}$ ratios on $ZrO_2(m)$ give the individual $k'_{\text{enolate,B}}$ and $k'_{\text{enolate,A}}$ values that combine to give the measured $k'_{\text{enolate,total}}$ values (eq 14) and depend on the respective free energy barriers ($\Delta G'^{\ddagger}_{\text{enolate}}$) for enolate formation on $Zr_A{-}O$ and $Zr_B{-}O$ pairs (eq 7). For ethanol−ethanal reactants, $\Delta G'^{\ddagger}_{\text{enolate}}$ values for $Zr_A{-}O$ and $Zr_B{-}O$ site pairs are 121 ± 1 and 124 ± 1 kJ mol^{-1}, respectively. The smaller barrier on $Zr_A{-}O$ pairs is consistent with the larger OH^- binding energy of Zr_A site (Scheme 6). Zr_A is a stronger acid than Zr_B and stabilizes the enolate TS through more effective interactions with the carbonyl O atom in alkanals than the weaker Zr_B centers. These $k'_{\text{enolate,B}}/k'_{\text{enolate,A}}$ ratios are similar for deuterated and undeuterated ethanol−ethanal reactants ($((k'_{\text{enolate,B}}/k'_{\text{enolate,A}})_H/(k'_{\text{enolate,B}}/k'_{\text{enolate,A}})_D = 1.2$; 523 K; Table 2), indicative of transition states that exhibit a similar extent of C−H bond breaking and O−H bond making on each of the $Zr_A{-}O$ and $Zr_B{-}O$ pairs.

We conclude that condensation and esterification elementary steps (Scheme 3) and their kinetic relevance are similar on $ZrO_2(m)$ and $TiO_2(a)$ surfaces but that selectivity descriptors must include the asymmetric nature of $Zr_A{-}O{-}Zr_B$ centers, absent for Ti−O−Ti structures. Detailed DFT descriptions of these selectivity trends require the use of periodic slab structures, because small cluster models that are appropriate for enolate formation on $ZrO_2(m)$ and $TiO_2(a)$ are able to capture the essential details required for selectivity predictions in the case of symmetric Ti−O−Ti structures (sections 3.5−3.9 and ref 30) but not for asymmetric $Zr_A{-}O{-}Zr_B$ species.[51]

3.3. Turnover Rates and Selectivities of Alkanol−Alkanal/Alkanone Mixtures.

Enolates form from two (or more) carbonyl compounds at rates which depend on their respective pressures at Ti−O or Zr−O site pairs on $TiO_2(a)$ and $ZrO_2(m)$ surfaces that remain essentially uncovered during steady-state catalysis (sections 3.1 and 3.2 and ref 30). Each enolate can then react with either one of the two carbonyl reactants to form four distinguishable condensation products and also with each alkanol present to form distinct esterification products.

For ethanol−1-propanol reactants on $TiO_2(a)$ + Cu/SiO_2 mixtures, the Cu function equilibrates ethanol−ethanal and 1-propanol−propanal reactants at each H_2 pressure; ethenolate (from ethanal) and propen-1-olate (from propanal) can each react with either ethanal or propanal to form butanal, pentanal, 2-methyl-butanal, and 2-methyl-pentanal (Scheme 8a); each of the two enolates also reacts with either ethanol or 1-propanol to form ethyl acetate, propyl acetate, ethyl propionate, and propyl propionate. Similarly, acetone−1-propanol reactants on $TiO_2(a)$ + Cu/SiO_2 mixtures form 2-methyl-pentanal, 2,3-dimethyl-butanal, 4-methyl-pentan-2-one, and hexan-2-one condensation products (Scheme 8b) and propyl propionate and isopropyl propionate as esterification products. The relative formation rates of these condensation and esterification products depend on the rates at which each carbonyl reactant forms its respective enolate and on the reactivity of the respective enolates toward each of the gaseous carbonyl or alkanol reactants. We examine here the ethanol−1-propanol and acetone−1-propanol reactants on $TiO_2(a)$ + Cu/SiO_2 mixtures as illustrative examples of cross-condensation and cross-esterification reactions, but the conclusions are also consistent with rate and selectivity data that we obtained for several mixtures of the other oxygenates used in this study.

Ethanol−1-propanol−H_2 reactants reached thermodynamic equilibrium with ethanal (C2al) and propanal (C3al) at all conditions on $TiO_2(a)$ + Cu/SiO_2 mixtures (1:1 mass; 523 K,

Table 3. $k_{C2al,i}K_{C2al}(k_{C3al,i}K_{C3al})^{-1}$ and $k_{C3one,i}K_{C3one}(k_{C3al,i}K_{C3al})^{-1}$ Obtained from Regression Fits of Rate Data and Corresponding ΔG Values for C_2 and C_3 Enolate reactants

enolate reactant	$k_{C2al,i}K_{C2al}(k_{C3al,i}K_{C3al})^{-1}$ [a]	$\Delta\Delta G^{\ddagger}_{C2al,i\text{-}C3al,i}$ [b] (kJ mol^{-1})	$k_{C3one,i}K_{C3one}(k_{C3al,i}K_{C3al})^{-1}$ [c]	$\Delta\Delta G^{\ddagger}_{C3one,i\text{-}C3al,i}$ [b] (kJ mol^{-1})
ethenolate	0.91 ± 0.03	0 ± 1		
propen-1-olate	0.89 ± 0.03	1 ± 1	<0.01	>20
propen-2-olate			0.0065 ± 0.0002	22 ± 1

[a] Data shown in Figure 8a. [b] Calculated using eq 24. [c] Data shown in Figure 8b.

20 kPa H_2; 0−2.0 kPa ethanol; 0−0.5 kPa 1-propanol). The conversion rates of each reactant did not depend on the presence or the concentration of the other reactant (section S5, SI), consistent with the low coverages of adsorbed intermediates prevalent during steady-state catalysis (section 3.1).

All four products expected from C−C coupling reactions of ethanal and propanal with ethenolate and propen-1-olate (Scheme 8a) were detected. For each given enolate i (i.e., ethenolate or propen-1-olate), the C−C coupling rates were proportional to the pressure of each carbonyl reactant (Figure 8a)

$$\frac{r_{m,i}}{r_{n,i}} = \frac{k_{m,i}K_m P_m}{k_{n,i}K_n P_n} \tag{23}$$

where $r_{m,i}$ and $r_{n,i}$ are the respective reaction rates of enolate i with carbonyl reactants m (C2al) and n (C3al) and $k_{m,i}$ and $k_{n,i}$ are the respective rate constants for these C−C coupling steps; K_m and K_n are the adsorption constants for m and n, respectively. The grouping of rate and adsorption constants in eq 23 is reflected in the slopes of the data shown in Figure 8a; these slopes depend on the difference between free energies of the two C−C coupling transition states and the respective gaseous alkanal reactants ($\Delta\Delta G^{\ddagger}_{m,i\text{-}n,i}$; m = C2al; n = C3al)

$$\frac{k_{m,i}K_m}{k_{n,i}K_n} = \exp\left(-\frac{\Delta\Delta G^{\ddagger}_{m,i-n,i}}{RT}\right) \tag{24}$$

$$\Delta\Delta G^{\ddagger}_{m,i-n,i} = G^{\ddagger}_{m,i} - G^{\ddagger}_{n,i} + G_n - G_m \tag{25}$$

where $G^{\ddagger}_{m,i}$ and $G^{\ddagger}_{n,i}$ are the free energies of the C−C coupling transition state of enolate i with carbonyl reactants m and n and G_m and G_n are the free energies of gaseous m and n.

Measured $\Delta\Delta G^{\ddagger}_{C2al,i\text{-}C3al,i}$ values (523 K; eq 24) for reactions of ethanal and propanal with ethenolate species were essentially zero (±1 kJ mol^{-1}; Table 3), indicative of their very similar reactivity. Propanal and ethanal reacted with propen-1-olate also at similar rates ($\Delta\Delta G^{\ddagger}_{C2al,i\text{-}C3al,i} = 1 \pm 1$ kJ mol^{-1}; Figure 8a; Table 3). These reactivities indicate that nucleophilic attack by enolates on alkanals depends only weakly on the alkyl substituents at the α-C atom in alkanals, consistent with the DFT results discussed in section 3.9.

The four distinct esters expected from C−O coupling of ethanol (C2ol) and 1-propanol (C3ol) with ethenolate and propen-1-olate were detected. The C−O coupling rate for each given enolate i (i.e., ethenolate or propen-1-olate) was proportional to the pressure of each alkanol coreactant (section S6, SI)

$$\frac{r_{M,i}}{r_{N,i}} = \frac{k_{M,i}K_{H-M,i}K_M P_M}{k_{N,i}K_{H-N,i}K_N P_N} \tag{26}$$

Here, $r_{M,i}$ and $r_{N,i}$ are the respective rates of enolate i reactions with 1-alkanols M (C2ol) and N (C3ol), $K_{H\text{-}M,i}$ and $K_{H-N,i}$ are the equilibrium constants for the H transfer between each 1-alkanol and enolate i to form alkanal−alkoxide pairs (step 9, Scheme 3), $k_{M,i}$ and $k_{N,i}$ are the rate constants for each subsequent alkanal−alkoxide C−O coupling (step 10, Scheme 3), and K_M and K_N are the adsorption constants of M and N, respectively. The grouping of rate and adsorption constants in eq 26 reflects the free energy difference between the two C−O coupling transition states and the respective gaseous alkanol reactants ($\Delta\Delta G^{\ddagger}_{M,i\text{-}N,i}$; M = C2ol; N = C3ol)

$$\frac{k_{M,i}K_{H-M,i}K_M}{k_{N,i}K_{H-N,i}K_N} = \exp\left(-\frac{\Delta\Delta G^{\ddagger}_{M,i-N,i}}{RT}\right) \tag{27}$$

$$\Delta\Delta G^{\ddagger}_{M,i-N,i} = G^{\ddagger}_{M,i} - G^{\ddagger}_{N,i} + G_N - G_M \tag{28}$$

where $G^{\ddagger}_{M,i}$ and $G^{\ddagger}_{N,i}$ are the free energies of the C−O coupling transition states for enolate i with 1-alkanols M and N and G_M and G_N are the free energies of gaseous M and N. Measured $\Delta\Delta G^{\ddagger}_{C2ol,i\text{-}C3ol,i}$ values (523 K; eq 28) for both ethenolate and propen-1-olate were nearly zero (±1 and ±1 kJ mol^{-1}; section S6, SI). These data show that different enolates react at similar rates in C−O coupling reactions with 1-alkanols; such similar rates reflect the very weak effects of alkyl chains in 1-alkanols on the stability of the TS that mediates C−O bond formation.

Hydrogenation−dehydrogenation equilibrium also prevailed at all conditions for acetone (0−2.0 kPa) and 1-propanol (0−1.0 kPa) mixtures on $TiO_2(a)$ + Cu/SiO_2 catalyst mixtures (1:1 mass; 523 K, 20 kPa H_2), and conversion rates for each carbonyl reactant were independent of the presence or concentration of the other (section S5, SI). Acetone (C3one) and propanal (C3al) reactions with propen-2-olate (from acetone) were proportional to the respective pressures of each carbonyl reactant (Figure 8b), as expected from the pathways depicted in Scheme 8b and consistent with eq 23 (m = C3one; n = C3al). The slope of the regressed trend line in Figure 8b ($k_{C3one,i}K_{C3one}$ $(k_{C3al,i}K_{C3al})^{-1}$ in eq 23) reflects the free energies of the transition states for C−C coupling between the enolate i and the two carbonyl compounds and the respective free energies of the carbonyl reactants as gaseous molecules ($\Delta\Delta G^{\ddagger}_{C3one,i\text{-}C3al,i}$; eqs 24 and 25).

The measured $\Delta\Delta G^{\ddagger}_{C3one,i\text{-}C3al,i}$ value for reactions of acetone and propanal with propen-2-olate was 22 ± 1 kJ mol^{-1} (523 K; Table 3), indicative of the much more reactive nature of alkanals than alkanones as reactants for each given enolate, as also found for their reactions with propen-1-olates species derived from propanal ($\Delta\Delta G^{\ddagger}_{C3one,i\text{-}C3al,i} > 20$ kJ mol^{-1}, a limit set by chromatographic detection). The steric effects are imposed by the additional $-CH_3$ group at the carbonyl C atom in acetone (vs the H atom in propanal); they offset the higher nucleophilic reactivity expected from the more electrophilic nature of the additional $-CH_3$ group in acetone. Such effects are confirmed and accurately described by the DFT-derived $\Delta\Delta G^{\ddagger}_{C2al,i\text{-}C3al,i}$ and $\Delta\Delta G^{\ddagger}_{C3one,i\text{-}C3al,i}$ values reported in section 3.9.

Scheme 9. Reaction Network of Aldol Condensation for Mixtures of Ethanal, Butanal, and Acetone Reactants on Bifunctional $TiO_2(a)$ + Cu/SiO_2 Catalysts

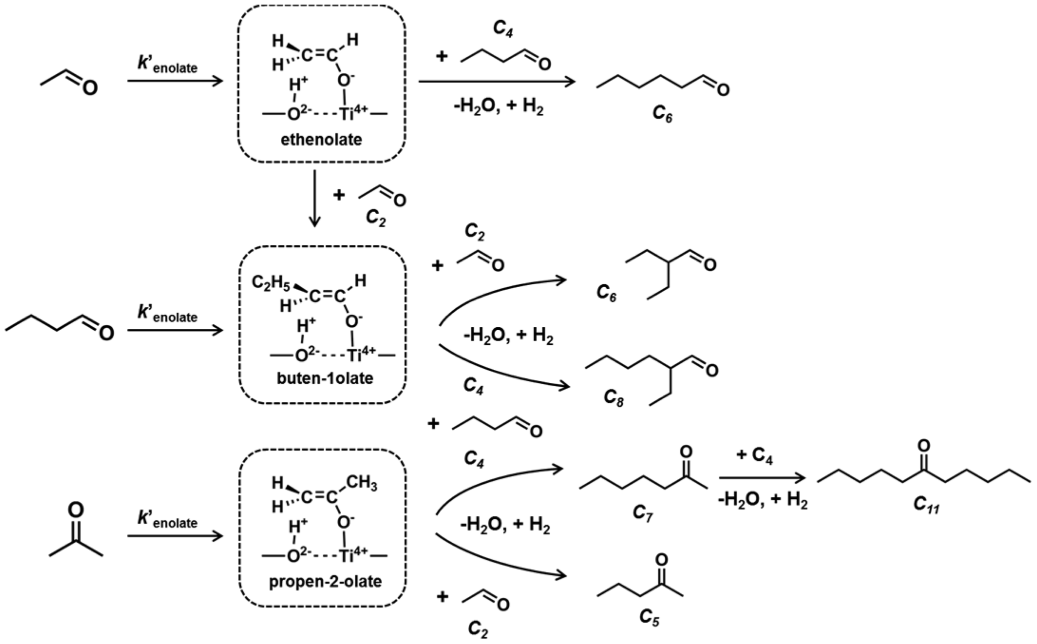

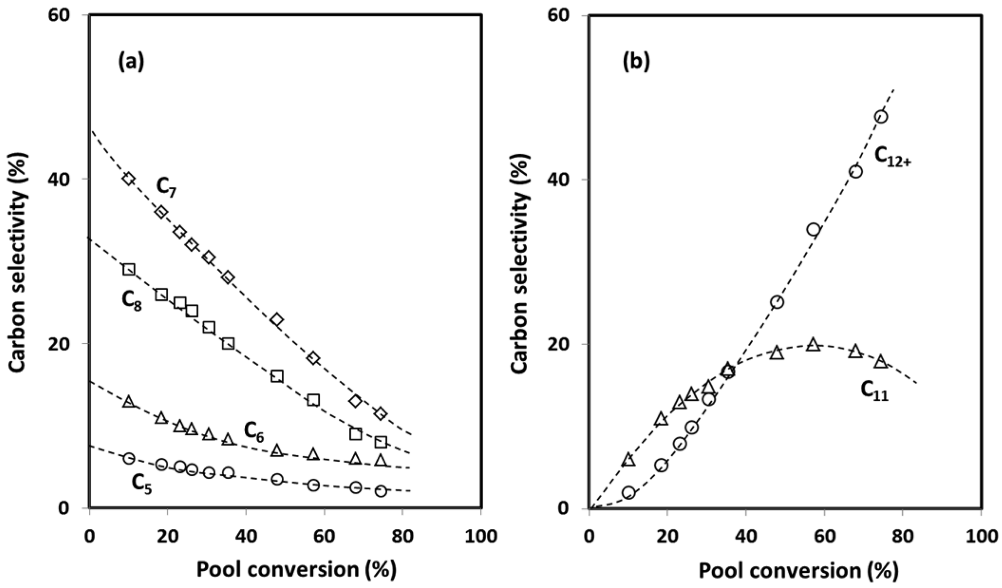

Figure 9. Carbon selectivities for (a) $C_{\leq 8}$ and (b) C_{9+} products as a function of pool conversion for acetone−1-butanol−ethanol reactant feeds (2.6 kPa acetone, 4.2 kPa 1-butanol, 2.2 kPa ethanol, 20 kPa H_2) on $TiO_2(a)$ + 20% wt Cu/SiO_2 mixtures (1:1 mass) at 523 K. Dashed curves indicate trends. Combined selectivities to C_{1-4} and C_{9-10} products (not included here) did not exceed 5%.

These mechanistic conclusions were also evident from the rates and selectivities measured with acetone−butanal−ethanal reactant mixtures, typical of those formed in ABE fermentation processes,[8] on $TiO_2(a)$ + Cu/SiO_2 mixtures (1:1 mass; 523 K, 20 kPa H_2; acetone:1-butanol:ethanol = 2.6:4.2:1.1 kPa). The molecular speciation and selectivities of the products formed were consistent with those independently measured from condensation and esterification reactions of each of the individual reactants involved. Specifically, conversion rates of each species were proportional to the pressure of each alkanone/alkanal and independent of the presence or concentration of the other reactants. The enolates formed from each carbonyl reactant preferentially reacted with butanal and ethanal, instead of acetone, to form C_5−C_8 condensation products (Scheme 9) and with the respective alkanols to form C_5−C_8 esters. The selectivity to these primary condensation and esterification products decreased monotonically as the conversion of the reactant pool increased with increasing residence time (Figure 9a) along with a concomitant increase in the selectivity to C_{9+} products formed in secondary condensation and esterification reactions (Figure 9b).

The average carbon number in the effluent stream (products and unconverted reactants) increased from 3.4 in reactants to 6.6 at 85% pool conversion (Figure 10a); the O/C ratio of the molecules in the effluent stream concomitantly decreased from 0.30 to 0.13 within the same conversion range (Figure 10b).

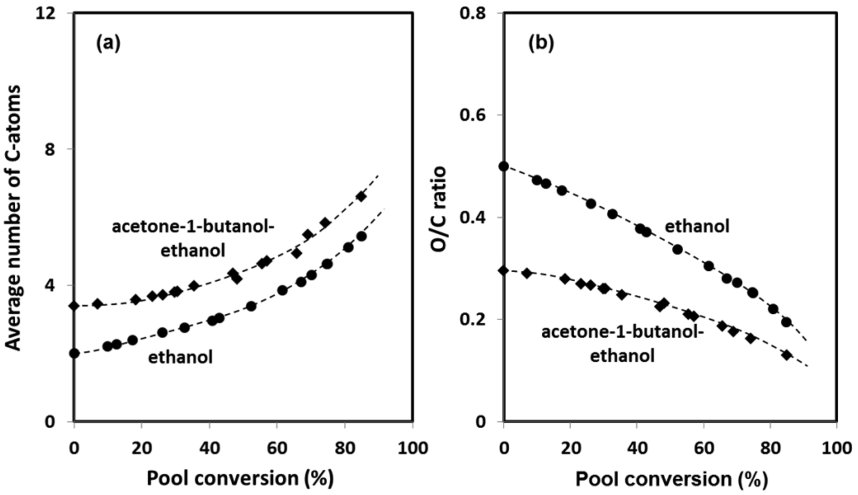

Figure 10. Average number of (a) C atoms and (b) O/C ratio of liquid effluents as a function of pool conversion for acetone−1-butanol−ethanol (2.6 kPa acetone, 4.2 kPa 1-butanol, 2.2 kPa ethanol, 20 kPa H_2) and ethanol reactant feeds (0.8 kPa ethanol and 40 kPa H_2) on $TiO_2(a)$ + 20% wt Cu/SiO_2 mixtures (1:1 mass) at 523 K. Dashed curves indicate trends.

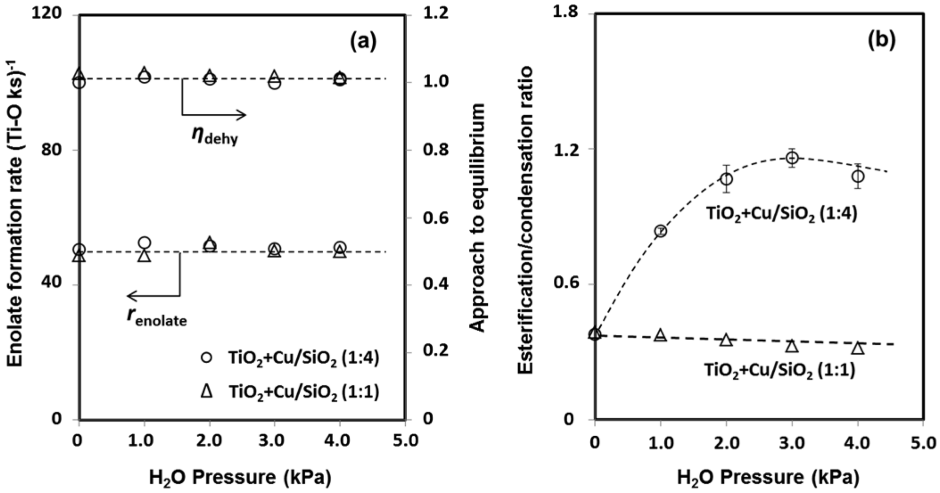

Figure 11. Effects of H_2O pressure on (a) approach to equilibrium factor for 1-propanol−propanal interconversions (η_{dehy}; eq 4) and enolate formation rates ($r_{enolate}$) and (b) ratios of esterification and condensation rates for 1-propanol−propanal reactants ($TiO_2(a)$ + 20% wt Cu/SiO_2 (1:1 or 1:4 mass), 523 K, 4 kPa 1-propanol, 40 kPa H_2). Dashed lines indicate trends.

Such trends resemble those observed for pure ethanol−ethanal mixtures (Figure 10) on $TiO_2(a)$ + Cu/SiO_2 mixtures (1:1 mass; 523 K, 0.8 kPa ethanol, 40 kPa H_2). For these mixtures, the average carbon number in the effluent stream increased from 2.0 in reactants to 5.4 at 85% pool conversion (Figure 10a), while the O/C ratio concurrently decreased from 0.50 to 0.19 (Figure 10b).

3.4. Effects of H_2O on 1-Alkanol Turnover Rates and Selectivities.

Condensation reactions form H_2O and α,β-unsaturated carbonyl molecules in equimolar amounts (Scheme 2), leading to H_2O as a significant coproduct. H_2O may influence enolate formation or reaction rates through competitive molecular or dissociative binding onto acid−base site pairs or via interactions with enolates; H_2O could also affect the Cu function by inhibiting hydrogenation−dehydrogenation reactions.

We examine here such effects of H_2O for 1-propanol reactants on two bifunctional $TiO_2(a)$ + Cu/SiO_2 mixtures with different ratios of the two functions (1:1 or 1:4 mass; 523 K; 40 kPa H_2). The forward rates of 1-propanol dehydrogenation to propanal on monofunctional Cu/SiO_2 catalysts decreased slightly (from 0.19 to 0.15 μmol $g_{Cu/SiO2}^{-1}s^{-1}$) with increasing H_2O pressure (from 0.1 to 4 kPa; 523 K, 4.0 kPa 1-propanol, 20 kPa H_2, section S7, SI), consistent with weak inhibition of the Cu function. These experiments were carried out at much higher space velocities (>1.2 mmol $g_{Cu/SiO2}^{-1}$ s^{-1}) to prevent full hydrogenation−dehydrogenation equilibrium (η_{dehy} < 0.25). Such H_2O pressures did not preclude 1-propanol−propanal−H_2 equilibration within the catalyst bed at lower space velocities on either $TiO_2(a)$ + Cu/SiO_2 mixture (1:1 or 1:4 mass; η_{dehy} 0.9−1, Figure 11a). Enolate formation rates did not depend on H_2O pressure (Figure 11a), indicating that H_2O did not interfere with their kinetically relevant step and that equilibrated propanal pressures were established near the entrance of the catalyst bed even in the presence of H_2O. These negligible H_2O coverages on $TiO_2(a)$ surfaces are consistent with the moderate strength of the acid and base moieties in Ti−O site pairs, evident from the weak effects of pyridine and CO_2 titrants on enolate formation rates and from

Scheme 10. Proposed Pathway of the C−O Coupling between Enolates and H_2O on Ti−O−Ti Surface Structures (R = H or alkyl)

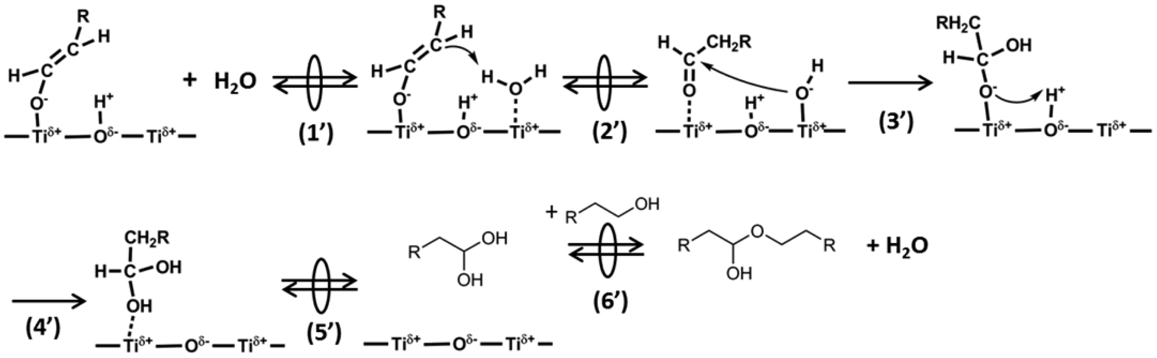

Scheme 11. DFT-Derived Structures Involved in Enolate Formation of Ethanal[a]

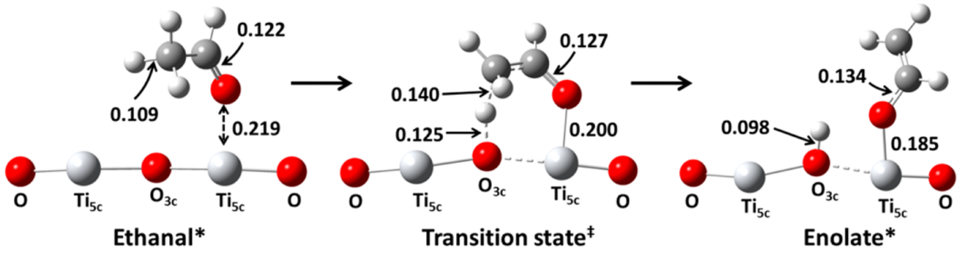

[a] On Ti_{5c}−O_{3c}−Ti_{5c} structures of the anatase $Ti_5O_{19}H_{18}$ cluster, B3LYP, 6-311G(d,p) for C, H, and O atoms, LANL2DZ for Ti atoms; only Ti_{5c}−O_{3c}−Ti_{5c} sites and two O atoms directly bound to the Ti_{5c} sites are shown for clarity. Distances are reported in nanometers.

theoretical treatments of the binding energies of OH^- and H^+ species formed via H_2O dissociation on $TiO_2(a)$ surfaces.[30]

In contrast, esterification/condensation rate ratios on $TiO_2(a)$ + Cu/SiO_2 (1:4 mass) increased from 0.38 to 1.2 as the prevalent H_2O pressure increased from 0.03 (2% conversion; mean bed value; no H_2O added) to 3 kPa (added H_2O) and reached nearly constant values before a slight decrease at higher pressures (4 kPa) (Figure 11b). Such effects, without any concomitant changes in conversion rates, indicate that H_2O favors C−O over C−C coupling reactions of the enolates to form hemiacetals. The weakening and ultimate reversal of such a preference reflect an inhibition of the Cu dehydrogenation function, required to scavenge hemiacetals to stable esters, at higher H_2O pressures (Scheme 3; section S7, SI); this is also shown by the monotonic effects of H_2O pressure on these rate ratios for $TiO_2(a)$ + Cu/SiO_2 mixtures with lower Cu contents (1:1 mass ratio; Figure 11b). H_2O and Cu contents can therefore be used in practice to control the relative rates of esterification and condensation for equilibrated 1-alkanol−alkanal reactants on bifunctional systems with Cu and $TiO_2(a)$ functions.

The strong promoting effects of H_2O on esterification selectivity, evident on the catalyst mixtures with higher Cu contents (Figure 11b), indicate that H_2O can increase esterification rates by decreasing the activation barrier to form C−O coupling products in enolate−1-propanol pairs. Enolates can react with H_2O to form 1,1-diols on Ti−O site pairs (steps 1′−5′, Scheme 10) in reactions analogous to those that form new C−O bonds via coupling of enolates with alkanols (HOH vs ROH in Scheme 3). Subsequent etherification reactions of these diols with 1-propanol (step 6′, Scheme 10) then form the same hemiacetal as in the direct C−O coupling of the enolate−1-propanol pair but apparently at higher rates as the result of the action of H_2O as a cocatalyst.

DFT calculations on $Ti_5O_{19}H_{18}$ cluster models show that the C−O coupling TS of the propanal−hydroxyl pair gives the highest free energy along the proposed enolate−H_2O reaction pathway at Ti−O−Ti surface structures (section S13, SI), suggesting that C−O coupling steps limit enolate−H_2O reactions, as also found for the analogous enolate−alkanol esterification route (section 3.1). The free energy of this propanal−hydroxyl C−O coupling TS is lower than for the propanal−1-propoxide C−O coupling TS involved in the propen-1-olate−1-propanol reaction by 21 kJ mol^{-1} (section S13, SI), consistent with the proposed catalytic role of H_2O in hemiacetal formation. Therefore, H_2O, albeit at concentrations significantly higher than those prevalent at the low conversions of this mechanistic study, leads to a preference for esterification routes (Figure 11b). Such promotion requires, however, high Cu contents in catalyst mixtures, because H_2O also inhibits dehydrogenation steps required for hemiacetal conversion to esters, thus creating a thermodynamic bottleneck for any hemiacetal formation route, irrespective of kinetic preferences or the involvement of H_2O.

3.5. Theoretical Assessment of Condensation and Esterification Pathways on $Ti_5O_{19}H_{18}$ Clusters.

The mechanistic inferences from the previous sections are confirmed here by determining free energy barriers for the elementary steps in Scheme 3 on $Ti_5O_{19}H_{18}$ cluster models. These clusters contain Ti (Ti_{5c} and Ti_{6c}, Scheme 1) and O (O_{2c} and O_{3c}, Scheme 1) centers with the same coordination as those exposed on the predominant (101) surfaces of $TiO_2(a)$. Ti_{5c}−O_{3c}−Ti_{5c} surface structures are more active than the other structures for enolate formation and for subsequent coupling reactions of C_3 oxygenates because of their moderate acid−base strength and the suitable distances between the O site and the two Ti centers; these coupling reactions are required to complete condensation and esterification turnovers.[30] Similar

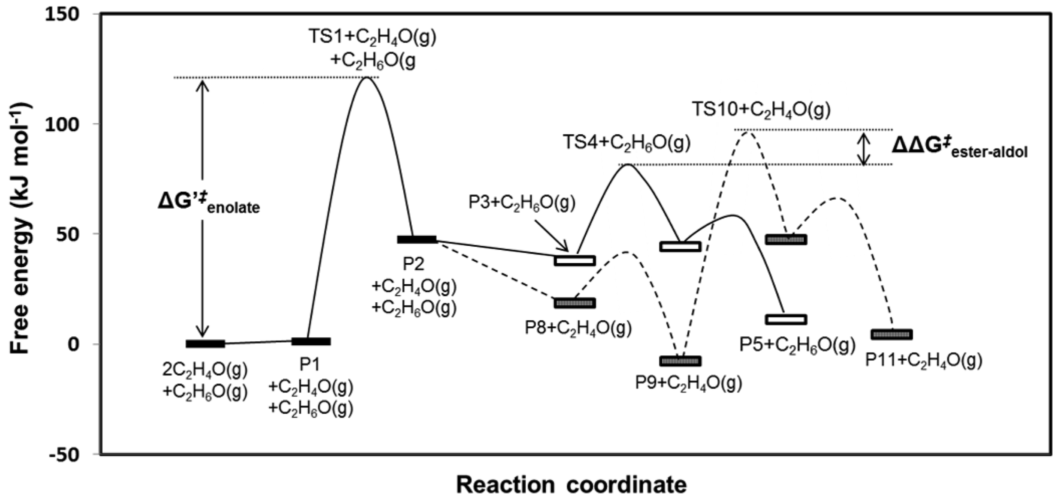

Figure 12. DFT-derived reaction free energy diagram of aldol condensation (solid lines) and esterification (dashed lines) for ethanol−ethanol reactants (on $Ti_{5c}-O_{3c}-Ti_{5c}$ structures of the anatase $Ti_5O_{19}H_{18}$ cluster, B3LYP, 6-311G(d,p) for C, H, and O atoms, LANL2DZ for Ti atoms; 523 K, 1 bar). TSj and Pj notations represent the respective transition state and product of step j in Scheme 3. Free energies are relative to a bare cluster and respective gaseous ethanal (C_2H_4O) and ethanol (C_2H_6O) reactants.

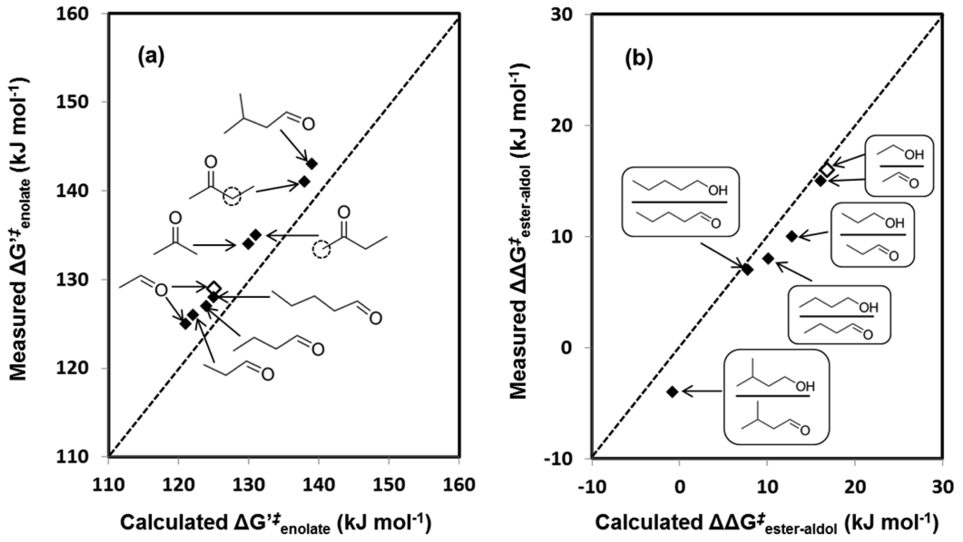

Figure 13. Measured and DFT-derived (a) $\Delta G'^{\ddagger}_{\text{enolate}}$ and (b) $\Delta\Delta G^{\ddagger}_{\text{ester-aldol}}$ for alkanals and alkanones (◆) $C_nH_{2n}O$, (◇) $C_nD_{2n}O$ ($n = 2-5$) (on $Ti_{5c}-O_{3c}-Ti_{5c}$ structures of the anatase $Ti_5O_{19}H_{18}$ cluster, B3LYP, 6-311G(d,p) for C, H, and O atoms, LANL2DZ for Ti atoms; 523 K, 1 bar). Data points for propanal and acetone adapted from ref 30. Dashed lines represent the parity lines.

conclusions were reached for reactions of C_2-C_5 carbonyl molecules (section 3.1) in general, and these $Ti_{5c}-O_{3c}-Ti_{5c}$ surface structures are used throughout the DFT treatments that follow.

DFT-derived structures for enolate formation steps from ethanal (step 2, Scheme 3) show that (i) the adsorbed ethanal (ethanal*) binds to a Ti_{5c} Lewis acid center via its carbonyl O atom ($Ti_{5c}-O$ 0.219 nm, Scheme 11), (ii) an α-H atom in ethanal* is abstracted by a basic O_{3c} site (α-H−O_{3c} 0.125 nm, Scheme 11), while the organic moiety is stabilized by the Ti_{5c} center ($Ti_{5c}-O$ 0.200 nm, Scheme 11) at the enolate formation TS, and (iii) the α-H−O_{3c} and $Ti_{5c}-O$ distances at the TS become shorter (0.098 and 0.185 nm, respectively; Scheme 11) as enolates form. The α-C−H bond at the TS (0.140 nm, Scheme 11) is longer than in ethanal* (0.109 nm) but much shorter than the combined van der Waals radii of the C and H atoms (0.29 nm), suggesting that the enolate formation TS occurs at an intermediate point along the reaction coordinate. The concerted and intermediate character of these transition states thus requires an appropriate balance of acid and basic strength at Ti−O site pairs. The intermediates and transition states involved in enolate formation (Scheme 11) and in its subsequent reactions (section S8, SI; Scheme 3) resemble those involved in similar reactions of propanal and acetone,[30] suggesting their general involvement in condensation and esterification reactions on acid−base site pairs at metal oxide surfaces.

Gibbs free energies of formation for the DFT-derived structures involved in ethanol−ethanal reactions (Scheme 3) on $Ti_{5c}-O_{3c}-Ti_{5c}$ surface structures are shown in Figure 12. All free energies (and those in sections 3.6−3.9) are referenced to a bare $Ti_5O_{19}H_{18}$ cluster and to the respective gaseous carbonyl or 1-alkanol reactants (at 523 K and 1 bar); the individual enthalpy and entropy components of these free energies are reported in the SI (section S8).

Table 4. DFT-Derived ΔG_{ads}, $\Delta G^{\ddagger}_{enolate}$, and $\Delta G'^{\ddagger}_{enolate}$ Values, Corresponding Enthalpy (ΔH) and Entropy ($-T\Delta S$) Contributions for Enolate Formation, and Deprotonation Enthalpies (ΔH_{DPE}) for Gaseous C_2−C_5 Carbonyl Alkanals and Alkanones[a]

	adsorption energy (kJ mol^{-1})			enolate formation barrier (kJ mol^{-1})				
reactant[b]	ΔH	$-T\Delta S$	ΔG	$\Delta H^{\ddagger}$	$-T\Delta S^{\ddagger}$	$\Delta G^{\ddagger}$	$\Delta G'^{\ddagger}_{enolate}$ (kJ mol^{-1})	ΔH_{DPE} (kJ mol^{-1})
$C^{\#}H_3CHO$	−88	89	1	105	15	120	121	1565
$CH_3C^{\#}H_2CHO$	−92	93	1	101	20	121	122	1557
$CH_3CH_2C^{\#}H_2CHO$	−97	96	−1	107	18	125	124	1547
$CH_3(CH_2)_2C^{\#}H_2CHO$	−98	99	1	107	17	124	125	1545
$(CH_3)_2CHC^{\#}H_2CHO$	−94	99	5	114	20	134	139	1556
$CH_3COC^{\#}H_3$	−92	97	4	109	17	126	130	1575
$CH_3CH_2COC^{\#}H_3$	−94	99	5	113	13	126	131	1568
$CH_3C^{\#}H_2COCH_3$	−94	99	5	114	19	133	138	1583

[a] On Ti_{5c}−O_{3c}−Ti_{5c} structures of the anatase $Ti_5O_{19}H_{18}$ cluster, B3LYP, 6-311G(d,p) for C, H, and O atoms, LANL2DZ for Ti atoms; 523 K, 1 bar. [b] α-C atoms from which a H atom is abstracted in the formation of the enolate are indicated by the pound sign ($^{\#}$).

The activation of the α-H atom in ethanal on Ti−O site pairs forms enolates in the elementary step with the highest free energy barrier along the condensation and esterification reaction coordinates (Figure 12). This elementary reaction thus represents the sole and common kinetically relevant step for both reactions. DFT-derived $\Delta G'^{\ddagger}_{enolate}$ values (121 kJ mol^{-1}, Figure 13a) and kinetic isotope effects ($(k'_{enolate})_H/(k'_{enolate})_D$ = 2.4, Figure 13a) for ethanal agree well with measured values (125 ± 1 kJ mol^{-1} and 2.3, Table 1).

Among the subsequent steps, which determine the fate of the enolate species, the C−C coupling TS (step 4, Scheme 3) gives the highest free energy along the condensation path ($\Delta G^{\ddagger}_{C-C}$ 81 kJ mol^{-1}, Figure 12), while the C−O coupling TS in ethanal−alkoxide pairs (step 10, Scheme 3; formed via H transfer in ethenolate−ethanol pairs in step 9, Scheme 3) provides the highest barrier along the esterification reaction coordinate ($\Delta G^{\ddagger}_{C-O}$ 97 kJ mol^{-1}, Figure 12). These two transition states thus determine the ratio of esterification and condensation rates. DFT-derived $\Delta\Delta G^{\ddagger}_{ester\text{-}aldol}$ (16 kJ mol^{-1}, eq 12, Figure 13b) and $(k_{CO}K_{ol}K_H(k_{CC}K_{al})^{-1})_H/(k_{CO}K_{ol}K_H(k_{CC}K_{al})^{-1})_D$ values (1.2, eq 9, Figure 13b) for ethanol−ethanal reactants also agree well with their respective experimental values (15 ± 1 kJ mol^{-1} and 1.4, Table 1). These theory−experiment benchmarks indicate that the level of theory and the small cluster structures used here are adequate to describe the observed condensation and esterification reactions on $TiO_2(a)$ catalysts.

DFT-derived and measured values of $\Delta G'^{\ddagger}_{enolate}$ and $\Delta\Delta G^{\ddagger}_{ester\text{-}aldol}$ are also similar to each other for reactions of C_4 and C_5 carbonyl molecules (Figure 13), confirming the accurate and general nature of the mechanistic proposals derived from experiments. The different values of $\Delta G'^{\ddagger}_{enolate}$ and $\Delta\Delta G^{\ddagger}_{ester\text{-}aldol}$ among these oxygenate reactants (Figure 13) reflect the effects of molecular identity on enolate formation rates and on C−C/C−O coupling selectivities, respectively. The quantitative analysis of these molecular effects on reactivity in terms of DFT-derived enthalpy and entropy values is discussed below (sections 3.6−3.9).

3.6. Theoretical Assessment of Alkyl Substituent Effects on Enolate Formation Rates on Ti−O Site Pairs.

The value of $\Delta G'^{\ddagger}_{enolate}$ represents the combined free energy change upon adsorption of a gaseous carbonyl molecule onto a Ti−O site pair (ΔG_{ads}) and the formation of the α-C−H bond cleavage TS from the adsorbed precursor ($\Delta G^{\ddagger}_{enolate}$; Scheme 4)

$$\Delta G'^{\ddagger}_{enolate} = \Delta G_{ads} + \Delta G^{\ddagger}_{enolate} \tag{29}$$

The DFT-derived enthalpy (ΔH) and entropy ($-T\Delta S$) contributions to ΔG_{ads} and $\Delta G^{\ddagger}_{enolate}$ values for C_2−C_5 carbonyl reactants are shown in Table 4. For linear alkanals, ΔH_{ads} values become more negative (from −88 to −98 kJ mol^{-1}) as alkyl chains lengthen (from ethanal to pentanal) and interact more strongly with Ti−O site pairs through van der Waals interactions. In concert, the ($-T\Delta S_{ads}$) term becomes more positive, thus compensating these changes in ΔH_{ads} and leading to adsorption free energies that are essentially independent of chain length for linear alkanals (±1 kJ mol^{-1} ΔG_{ads} differences). Consequently, the $\Delta G'^{\ddagger}_{enolate}$ values that account for reactivity predominantly reflect concomitant changes in the activation free energy for the elementary step that forms the enolate from the adsorbed linear alkanals ($\Delta G^{\ddagger}_{enolate}$, eq 29). Such $\Delta G^{\ddagger}_{enolate}$ values increase with the size of the α-alkyl group for C_2−C_4 linear alkanals (121−125 kJ mol^{-1}, Table 4) but then decrease slightly for *n*-pentanal (124 kJ mol^{-1}, Table 4). These effects of α-alkyl groups on $\Delta G^{\ddagger}_{enolate}$ are discussed below in the context of their enthalpy ($\Delta H^{\ddagger}_{enolate}$) and entropy ($-T\Delta S^{\ddagger}_{enolate}$) components.

First, we compare the $\Delta H^{\ddagger}_{enolate}$ and ($-T\Delta S^{\ddagger}_{enolate}$) contributions to $\Delta G^{\ddagger}_{enolate}$ for propanal and ethanal reactants. $\Delta H^{\ddagger}_{enolate}$ values are smaller for propanal than ethanal (101 vs 105 kJ mol^{-1}, Table 4), consistent with a $-CH_3$ group at the α-C atom stabilizing the enolate TS via p−π conjugation at the incipiently formed C=C bond.[66] Such a trend is evident from the smaller deprotonation enthalpy (ΔH_{DPE}) for gaseous propanal than ethanal (1557 vs 1565 kJ mol^{-1}, Table 4). The $-CH_3$ group, however, also leads to larger ($-T\Delta S^{\ddagger}_{enolate}$) values (20 vs 15 kJ mol^{-1}, Table 4) because it imposes greater configurational rigidity along the carbon backbone during α-C−H bond cleavage; such constrained structures are evident from the increase in dihedral angles between the O−C_1 and the C_2−C_3 bonds along the reaction coordinate that converts adsorbed propanal (162°) to the propen-1-olate formation TS (177°; Scheme 12a). These compensating effects of the $-CH_3$ group on $\Delta H^{\ddagger}_{enolate}$ and ($-T\Delta S^{\ddagger}_{enolate}$) result in the similar reactivities of ethanal and propanal in the formation of their respective enolates ($\Delta G'^{\ddagger}_{enolate}$ 121 vs 122 kJ mol^{-1}, Table 4).

An additional $-CH_2-$ group in the chain attached to the α-C atom (e.g., propanal vs butanal) increased $\Delta H^{\ddagger}_{enolate}$ values from 101 to 107 kJ mol^{-1} (Table 4) and decreased $-T\Delta S^{\ddagger}_{enolate}$ from 20 to 18 kJ mol^{-1} (Table 4). The higher $\Delta H^{\ddagger}_{enolate}$ values contrast the trends observed between ethanol and propanal;

Scheme 12. DFT-Derived Structures of Adsorbed Reactants and Transition States Involved in Enolate Formation for (a) Propanal, (b) Butanal, and Butanone with α-C−H Bond Cleavage (c) at the Primary α-C Atom and (d) at the Secondary α-C Atom[a]

(a) Enolate formation from propanal

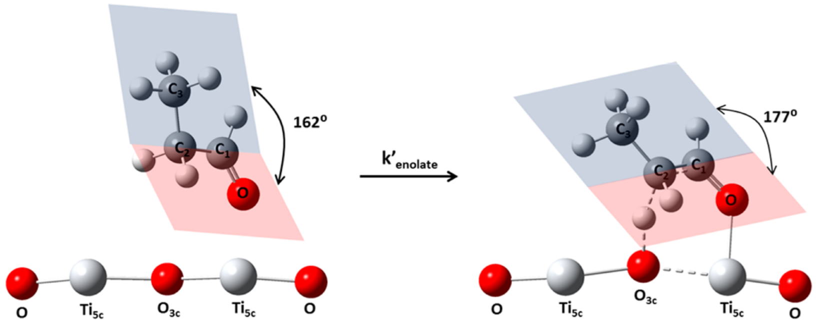

(b) Enolate formation from butanal

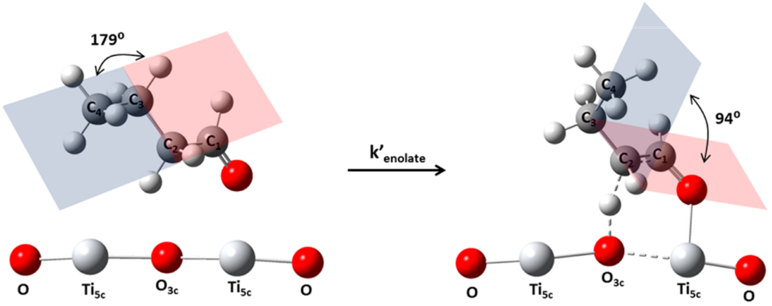

(c) Enolate formation from butanone (at the primary α-C-atom)

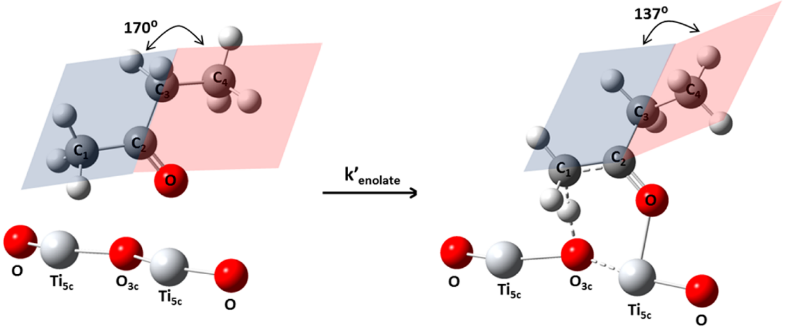

(d) Enolate formation from butanone (at the secondary α-C-atom)

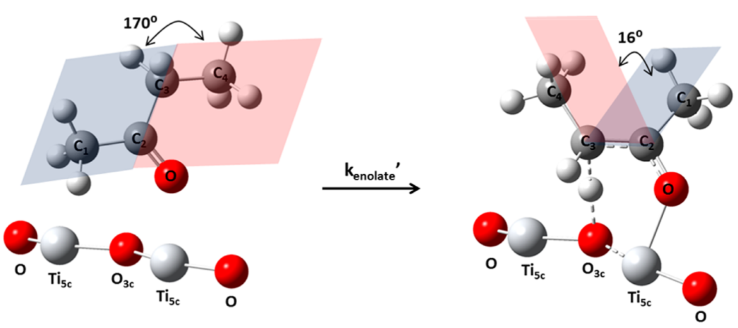

[a] On Ti_{5c}−O_{3c}−Ti_{5c} structures of the anatase $Ti_5O_{19}H_{18}$ cluster, B3LYP, 6-311G(d,p) for C, H, and O atoms, LANL2DZ for Ti atoms; only the Ti_{5c}−O_{3c}−Ti_{5c} sites and two O atoms directly bound to the Ti_{5c} sites are shown for clarity.

they reflect a significant distortion of the carbon backbone at the TS in order to avoid steric repulsion between the ethyl group and the Ti−O site pairs as the C−H bond is incipiently cleaved at the TS (Scheme 12b). Such trends are also found with further lengthening of a linear alkyl chain (pentanal; Table 4). We conclude that the higher $\Delta G'^{\ddagger}_{\text{enolate}}$ values and the lower reactivity observed for butanal relative to propanal (Figure 13) predominantly reflect steric effects caused by larger alkyls at the

Table 5. Bond Order of Chemical Bonds Involved in Enolate Formation Transition States for C_2−C_5 Alkanals and Alkanones[a]

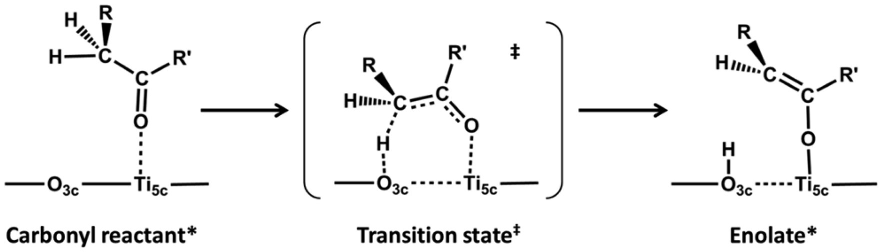

reactant[b]	α-C−H	α-H−O_{3c}	O−Ti_{5c}	C=O	C=C	Ti_{5c}−O_{3c}
$C^{\#}H_3CHO$	0.41	0.29	0.58	1.34	1.41	0.45
$CH_3C^{\#}H_2CHO$	0.39	0.27	0.61	1.31	1.40	0.45
$CH_3CH_2C^{\#}H_2CHO$	0.39	0.27	0.61	1.31	1.40	0.45
$CH_3(CH_2)_2C^{\#}H_2CHO$	0.39	0.27	0.61	1.31	1.41	0.45
$(CH_3)_2CHC^{\#}H_2CHO$	0.39	0.27	0.62	1.30	1.41	0.45
$CH_3COC^{\#}H_3$	0.38	0.30	0.62	1.26	1.41	0.43
$CH_3CH_2COC^{\#}H_3$	0.38	0.30	0.62	1.26	1.41	0.43
$CH_3C^{\#}H_2COCH_3$	0.37	0.29	0.65	1.24	1.39	0.43

[a] R, R′ = H or alkyl; on Ti_{5c}−O_{3c}−Ti_{5c} structures of the anatase $Ti_5O_{19}H_{18}$ cluster, B3LYP, 6-311G(d,p) for C, H, and O atoms, LANL2DZ for Ti atoms. [b] α-C atoms from which a H atom is abstracted in the formation of the enolate are indicated by the pound sign (#).

α-C atom. Indeed, 3-methyl butanal, in which the α-alkyl substituent is branched, gave a much larger $\Delta G'^{\ddagger}_{\text{enolate}}$ value than pentanal (139 vs 125 kJ mol^{-1}, Table 4); the branched alkyl group leads to less negative ΔH_{ads} values (by 4 kJ mol^{-1}) and to more positive $\Delta H^{\ddagger}_{\text{enolate}}$ values (by 7 kJ mol^{-1}) for 3-methyl-butanal than for the linear pentanal, even though both reactants contain the same number of C atoms (Table 4).

A second alkyl group at the carbonyl C atom (to give alkanones) makes adsorption less favorable (ΔG_{ads} less negative) because of repulsion between the additional alkyl and the Ti−O site pairs; it also leads to less stable enolate formation transition states relative to its adsorbed carbonyl precursors (lager $\Delta G^{\ddagger}_{\text{enolate}}$). These trends reflect a concomitant strengthening of the α-C−H bonds, as shown from the reactivity differences between acetone and propanal (Figure 13). Among alkanone reactants, butanone gave ΔG_{ads} and $\Delta G^{\ddagger}_{\text{enolate}}$ values (for activation at the terminal α-C atom) similar to those for acetone (Table 4), reflecting the similar effects of $-C_2H_5$ and $-CH_3$ species at the C=O group on the adsorbed intermediates and the TS as a result of their compensating effects on enthalpy (ΔH) and entropy ($-T\Delta S$) in their ΔG terms. Specifically, the butanone backbone distorts during α-C−H cleavage at its primary α-C atom, with dihedral angles between C_1−C_2 and C_3−C_4 bonds that decrease as the adsorbed reactant (170°) forms the enolate TS (137°; Scheme 12c). This change leads, in turn, to larger $\Delta H^{\ddagger}_{\text{enolate}}$ values (113 kJ mol^{-1}) but to smaller ($-T\Delta S^{\ddagger}_{\text{enolate}}$) values (13 kJ mol^{-1}) than for acetone reactants (109, 17 kJ mol^{-1}; Table 4). Such compensation effects are responsible for the similar reactivity and $\Delta G^{\ddagger}_{\text{enolate}}$ for butanone (at the terminal α-C atom) and acetone (Figure 13).

The activation of the secondary α-C atom in butanone gave significantly larger $\Delta G^{\ddagger}_{\text{enolate}}$ values than at the terminal α-methyl group (133 vs 126 kJ mol^{-1}, Table 4). These differences predominantly reflect their different ($-T\Delta S^{\ddagger}_{\text{enolate}}$) values (19 vs 13 kJ mol^{-1}, Table 4), caused by the loss of rotational freedom of the terminal $-CH_3$ groups located at the secondary α-C atom and the carbonyl C atom. These two $-CH_3$ groups are much closer to each other at the TS for the activation of the secondary α-C atom than at the TS for the activation of the terminal α-C atom, as shown by the smaller dihedral angle between the C_1−C_2 and the C_3−C_4 bonds in the TS for the secondary C atom than for the terminal α-C atom (16° vs 137°, Scheme 12c and 12d). The similar $\Delta H^{\ddagger}_{\text{enolate}}$ values at terminal and secondary α-C atoms in butanone (113 and 114 kJ mol^{-1}; Table 4) contrast their large ΔH_{DPE} differences (15 kJ mol^{-1}) between these two α-C atoms for the gaseous molecule (1568 and 1583 kJ mol^{-1}; Table 4). Their similar reactivity reflects the steric influence of the $-C_2H_5$ group as the TS for C−H cleavage at the terminal α-C atom interacts with vicinal O atoms on TiO_2 surfaces (Scheme 1). These findings highlight the pre-eminent role of steric effects as the relevant descriptor that complements the DPE values of gaseous reactants, typically used to predict molecular reactivity in condensation reactions catalyzed by liquid acids and bases.[67]

3.7. Molecular Descriptors and Brønsted−Evans−Polanyi Relations for Enolate Formation Reactivity.

The activation barriers for enolate formation from carbonyl reactants ($\Delta H^{\ddagger}_{\text{enolate}}$) depend on the heterolytic dissociation energies of their α-C−H bonds (ΔH_{DPE}) in formalisms typically known as the Brønsted−Evans−Polanyi (BEP) relations.[68] They also depend on steric effects imposed by the α-alkyl substituents at the enolate formation TS. Such steric effects, illustrated in section 3.6, are not inherently linked to the ΔH_{DPE} values for the gaseous reactants. Here, we examine $\Delta H^{\ddagger}_{\text{enolate}}$ values as a function of ΔH_{DPE} for C_2−C_5 carbonyl reactants to discern the relative contributions of ΔH_{DPE} and of steric effects to the stability of their respective enolate formation TS ($\Delta H^{\ddagger}_{\text{enolate}}$).

The sensitivity of $\Delta H^{\ddagger}_{\text{enolate}}$ to ΔH_{DPE} depends on the extent to which the C−H bond is cleaved at the enolate formation transition state.[68] This reflects, in turn, the lateness of the TS along the reaction coordinate, which can be defined as the number of shared electron pairs in the most plausible Lewis electronic structures.[48,49] Enolate formation on Ti_{5c}−O_{3c} site pairs involves the concerted cleavage of an α-C−H bond and the formation of a bond between the H abstracted and the O_{3c} site (α-H−O_{3c}) and between the carbonyl O atom and the Ti_{5c} center (O−Ti_{5c}). These changes occur concurrently with the transition of the carbonyl C=O bond into to a single C−O

DOI: 10.1021/acs.jpcc.6b07304
J. Phys. Chem. C 2016, 120, 21589−21616

bond, of the C−C bond in the carbonyl reactant into a C═C bond, and with the cleavage of the Ti_{5c}−O_{3c} bond (Scheme 11). For C_2−C_5 alkanals and alkanones, the orders of the α-C−H bond at the TS are similar (0.37−0.41; Table 5), as is the case also for the α-H−O_{3c} (0.27−0.30), O−Ti_{5c} (0.58−0.65), C═O (1.24−1.34), C═C (1.39−1.41), and Ti_{5c}−O_{3c} (0.43−0.45) bonds involved in the enolate formation TS (Table 5); these values are indicative of transition states similar in lateness along the reaction coordinate for all C_2−C_5 alkanals and alkanones. As a result, a nearly linear dependence between $\Delta H^{\ddagger}_{\text{enolate}}$ and ΔH_{DPE} is expected for all C_2−C_5 alkanals and alkanones in the absence of significant steric effects.

DFT-derived $\Delta H^{\ddagger}_{\text{enolate}}$ values for carbonyl reactants with short alkyl groups at the α-C atom (ethanal, propanal, acetone, butanone ($CH_3C^{\#}H_2COCH_3$)) are proportional to their respective ΔH_{DPE} values with a slope of 0.49 ± 0.03 (Figure 14), consistent with values expected for TS structures nearly equidistant between reactant and product states along the reaction coordinate. C_4 and C_5 alkanals with bulkier alkyls at their α-C atom, however, do not lie along the trend lines observed for the other alkanals (Figure 14); their TS structures are less stable, and the $\Delta H^{\ddagger}_{\text{enolate}}$ values are larger than predicted from their α-C atom DPE values. These deviations increase as the size of the pendant alkyl groups increases (11, 12, and 14 kJ mol^{-1} for butanal, pentanal, and 3-methylbutanal; Figure 14). These differences seem unrelated to the ability of such transition states to bind at Ti−O site pairs, because (i) the orders of the α-H−O_{3c} (0.27−0.30) and the O−Ti_{5c} (0.58−0.65) bonds at the TS are similar for all reactants (Table 5) and (ii) the carbonyl O atoms in C_4−C_5 alkanals are more strongly basic than for propanal (DFT-derived proton affinities: propanal −796 kJ mol^{-1}; butanal −810 kJ mol^{-1}; pentanal −816 kJ mol^{-1}; section S9, SI), leading to stronger binding at Ti centers for the C_4−C_5 enolate formation TS structures. Thus, we conclude that distortion at the TS relative to the structure of the gaseous reactants accounts for this strong destabilization.

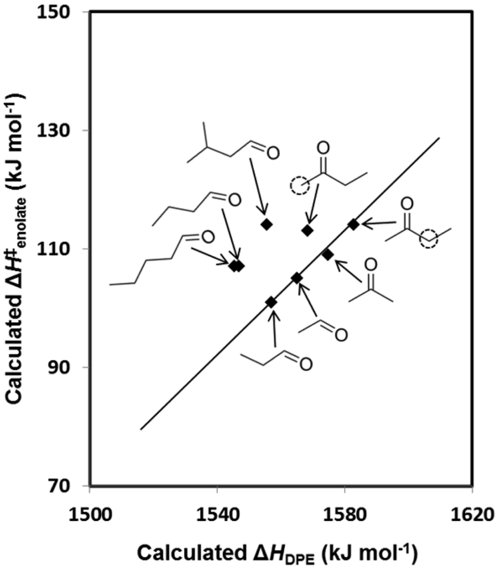

Figure 14. Correlation between DFT-derived ΔH_{DPE} and $\Delta H^{\ddagger}_{\text{enolate}}$ values for C_2−C_5 alkanals and alkanones (on Ti_{5c}−O_{3c}−Ti_{5c} structures of the anatase $Ti_5O_{19}H_{18}$ cluster, B3LYP, 6-311G(d,p) for C, H, and O atoms, LANL2DZ for Ti atoms; 523 K). Solid line represents a linear fit of the data for ethanal, propanal, acetone, and butanone (with a H atom abstracted from the secondary α-C atom in enolate formation).

Butanone activation at the terminal α-C−H position ($CH_3CH_2COC^{\#}H_3$) also deviates from the linear trends in Figure 14 (by 7 kJ mol^{-1}); these linear trends describe the activation of its secondary α-C atom, indicating that deviations from such trends reflect the distortion imposed by the pendant −C_2H_5 group attached at the carbonyl C atom. Such steric hindrance is weaker than that observed for a −C_2H_5 group at the α-C atom (butanal; 11 kJ mol^{-1}; Figure 14), because of the closer proximity of the −C_2H_5 group in butanal to the active Ti−O structures at the enolate formation TS.

These deviations from a universal relation between $\Delta H^{\ddagger}_{\text{enolate}}$ and ΔH_{DPE} (Figure 14) reflect the significant consequences of steric effects for reactivity on surfaces and the incomplete character of DPE values as sole molecular descriptors of reactivity. More complete descriptors must capture the lateness of the concerted transition states and the distortion required to accommodate concerted interactions with O and Ti surface atoms. These complexities, brought forth by the rigid nature of surfaces and by the distance requirements for incipiently formed O−Ti and H−O bonds, contrast the more general descriptions based solely on DPE values for enolate formation in condensation and esterification reactions catalyzed by liquid acids and bases.[67] Their description requires a level of theoretical treatment previously unavailable for these reactions on realistic surfaces.

3.8. Alkyl Substituent Effects on C−C and C−O Coupling of Enolates in Reactions of Alkanals and 1-Alkanols.

Esterification and condensation selectivities are determined by the relative rates of C−C bond formation in enolate−alkanal pairs and of C−O bond formation in the alkanal−alkoxide pairs formed via H transfer between enolates and 1-alkanols (section 3.5). For all C_2−C_5 alkanal−alkanol reactants, the length of the incipiently formed C−C bond at the C−C coupling TS is 0.213−0.220 nm, while that of the C−O bond at the C−O coupling TS is 0.173−0.184 nm (section S10, SI). The structures of the transition states that mediate condensation and esterification routes of enolates are similar for all reactants, irrespective of the backbone length or the extent of branching at their alkyl chains.

DFT-derived enthalpy ($\Delta H^{\ddagger}_i$) and entropy ($-T\Delta S^{\ddagger}_i$) contributions to $\Delta G^{\ddagger}_{\text{i}}$ (i = C−C for condensation or C−O for esterification) values for C_2−C_5 alkanals are shown in Table 6. $\Delta H^{\ddagger}_i$ values are also dissected into their quasi-classical van der Waals ($\Delta H_{\text{vdw},i}$) and residual quantum mechanical ($\Delta H^{\ddagger}_{\text{unc},i}$) components

$$\Delta H^{\ddagger}_i = \Delta H^{\ddagger}_{\text{unc},i} + \Delta H_{\text{vdw},i} \tag{30}$$

in order to probe the role of dispersion forces on TS stability. For C−C coupling, $\Delta H^{\ddagger}_{\text{unc,C−C}}$ values became less negative for larger alkyl chains (from −24 (ethanal) to −11 kJ mol^{-1} (pentanal)), indicative of the repulsive component included in the quantum mechanical treatments used to derive the magnitude of this term. Such repulsive interactions between the alkyl groups in the enolate−alkanal pair at the TS are also evident from the distance between the β-C atom in the enolates and the α-C atom in the alkanals (0.315 nm for propen-1-olate−propanal pairs; Scheme 13a), which is smaller than the combined van der Waals radii of these two C atoms (0.34 nm). These steric effects become more apparent for 3-methyl butanal reactants, which show nearly zero $\Delta H^{\ddagger}_{\text{unc,C−C}}$ values (Table 6).

Table 6. DFT-Derived Contributions of Enthalpy ($\Delta H^{\ddagger}_{unc,i}$), Dispersion Correction ($\Delta H_{vdw,i}$), and Entropy ($-T\Delta S^{\ddagger}_{i}$) to $\Delta G^{\ddagger}_{i}$ (i = C−C or C−O) and $\Delta\Delta G^{\ddagger}_{ester\text{-}aldol}$ for C_2−C_5 Alkanals[a]

alkanal reactant	ethanal	propanal	butanal	pentanal	3-methyl butanal
$\Delta H^{\ddagger}_{unc,C-C}$	−24	−21	−15	−11	0
$\Delta H_{vdw,C-C}$	−87	−104	−111	−116	−121
$-T\Delta S^{\ddagger}_{C-C}$	192	200	199	200	205
$\Delta G^{\ddagger}_{C-C}$	81	76	73	72	84
$\Delta H^{\ddagger}_{unc,C-O}$	1	−1	−1	0	0
$\Delta H_{vdw,C-O}$	−95	−106	−111	−116	−114
$-T\Delta S^{\ddagger}_{C-O}$	192	196	196	195	197
$\Delta G^{\ddagger}_{C-O}$	97	89	83	80	83
$\Delta\Delta H^{\ddagger}_{unc,ester\text{-}aldol}$	25	19	13	12	0
$\Delta\Delta H_{vdw,\ ester\text{-}aldol}$	−9	−2	0	1	7
$-T\Delta\Delta S^{\ddagger}_{ester\text{-}aldol}$	0	−4	−3	−5	−8
$\Delta\Delta G^{\ddagger}_{ester\text{-}aldol}$	16	13	10	8	−1

[a] Units: kJ mol^{-1}; on Ti_{5c}−O_{3c}−Ti_{5c} structures of the anatase $Ti_5O_{19}H_{18}$ cluster, B3LYP, 6-311G(d,p) for C, H, and O atoms, LANL2DZ for Ti atoms; 523 K, 1 bar.

The van der Waals interactions (ΔH_{vdw}) at the C−C coupling TS become stronger for larger alkyls (−87 (ethanal) and −121 kJ mol^{-1} (3-methyl butanal)). The $-T\Delta S^{\ddagger}_{C-C}$ term concurrently increases (192 (ethanal) and 205 kJ mol^{-1} (3-methyl butanal)), because of the more rigid configurations imposed by longer or bulkier alkyls. Free energy values for the enolate−carbonyl C−C coupling TS ($\Delta G^{\ddagger}_{C-C}$, relative to a bare $Ti_5O_{19}H_{18}$ cluster and gaseous alkanal/alkanone reactants) decrease as the backbone lengthens (from 82 to 71 kJ mol^{-1}) for linear C_2−C_5 alkanals, reflecting the stronger van der Waals interactions for larger bimolecular transition states; 3-methyl butanal gave larger $\Delta G^{\ddagger}_{C-C}$ values (84 kJ mol^{-1}, Table 6) than the linear alkanals, because steric repulsion offsets the benefits of van der Waals stabilization for the C−C coupling TS structures derived from 3-methyl butanal reactants.

In contrast with the C−C coupling TS structures, the alkyl groups at the C−O coupling TS analogs point away from each other (Scheme 13b), thus minimizing any steric effects. Indeed, $\Delta H^{\ddagger}_{unc,C-O}$ and $-T\Delta S^{\ddagger}_{C-O}$ are similar among all C_2−C_5 alkanals (Table 6). $\Delta H_{vdw,C-O}$ values, however, become more negative with increasing alkyl size (−95 (ethanal) and−116 kJ mol^{-1} (pentanal)), leading to a decrease in $\Delta G^{\ddagger}_{C-O}$ for longer backbones, as a result of the prevalent role of van der Waals interactions that favor the larger bimolecular C−O coupling transition states.

Table 6 lists the differences in the enthalpies uncorrected for van der Waals effects ($\Delta\Delta H^{\ddagger}_{unc,\ ester\text{-}aldol}$) and in the van der Waals interaction enthalpies ($\Delta\Delta H_{vdw,\ ester\text{-}aldol}$) and entropies ($-T\Delta\Delta S^{\ddagger}_{ester\text{-}aldol}$) involved in determining $\Delta G^{\ddagger}_{C-O}$ and $\Delta G^{\ddagger}_{C-C}$; their values determine, in turn, the relative esterification and condensation rates through $\Delta\Delta G^{\ddagger}_{ester\text{-}aldol}$ values (eq 12). In contrast with the individual $\Delta G^{\ddagger}_{C-O}$ and $\Delta G^{\ddagger}_{C-C}$ components, $\Delta\Delta G^{\ddagger}_{ester\text{-}aldol}$ predominantly reflects the $\Delta\Delta H^{\ddagger}_{unc,ester\text{-}aldol}$ term, because of the ubiquitous compensation

Scheme 13. DFT-Derived Transition State Structures of (a) C−C Coupling and (b) C−O Coupling Reactions for 1-Propanol-Propanal Reactions, of (c) C−C Coupling between Acetone and Propen-1-olate (derived from propanal), and of (d) C−C Coupling between Propanal and Propen-2-olate (derived from acetone)[a]

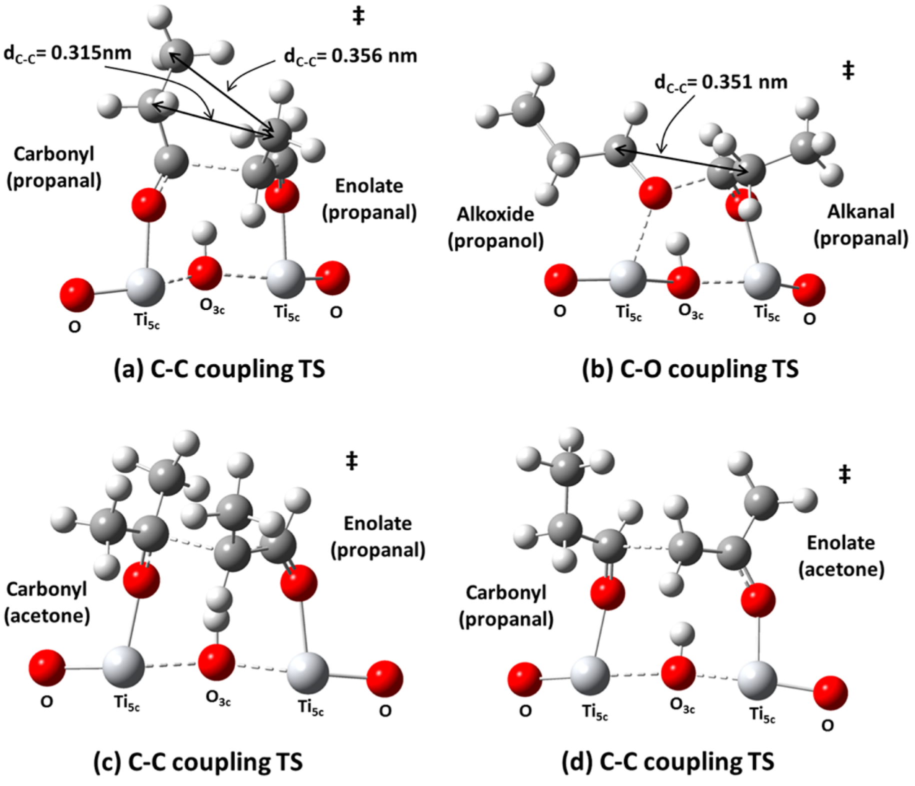

[a] On Ti_{5c}−O_{3c}−Ti_{5c} structures of the anatase $Ti_5O_{19}H_{18}$ cluster, B3LYP, 6-311G(d,p) for C, H, and O atoms, LANL2DZ for Ti atoms; only the Ti_{5c}−O_{3c}−Ti_{5c} sites and two O atoms directly bound to the Ti_{5c} sites are shown for clarity.

between $\Delta\Delta H_{\text{vdw,ester-aldol}}$ and $\Delta\Delta S^{\ddagger}_{\text{ester-aldol}}$. As a result, the esterification and condensation selectivities depend most sensitively on the different repulsive interactions between the alkyl groups at the C−C and C−O coupling transition states; these observations predominantly reflect the different orientations of these alkyl groups with respect to each other in the C−C and C−O bond formation TS structures (Scheme 13a and 13b).

3.9. Relative Reactivities of Carbonyl and Enolate Reactants in C−C Coupling Reactions.

The reactivity of different carbonyl reactants with a given enolate depends on their different $\Delta G^{\ddagger}_{\text{C−C}}$ values, referenced to the gaseous reactant and the given bound enolate (Scheme 5). $\Delta\Delta G^{\ddagger}_{\text{C2al},i\text{-C3al},i}$ (eq 25; m = C2al, n = C3al) values reflect the $\Delta G^{\ddagger}_{\text{C−C}}$ difference between C−C coupling reactions of ethanal and propanal with a given enolate i. DFT-derived $\Delta\Delta G^{\ddagger}_{\text{C2al},i\text{-C3al},i}$ values for reactions of ethanol and propanal with ethenolates and propen-1-olates are 3 and 1 kJ mol^{-1}, respectively (Table 7), in agreement with measurements (±1 and 1 ± 1 kJ mol^{-1}, Table 3). $\Delta\Delta G^{\ddagger}_{\text{C3one},i\text{-C3al},i}$ values (eq 25; m = C3one, n = C3al) represent the difference in $\Delta G^{\ddagger}_{\text{C−C}}$ for reactions of a given enolate i with acetone and propanal. Their values are large and similar (21 kJ mol^{-1}; Table 7) for reactions with propen-1-olates and propen-2-olates, consistent with the observed preference of all enolates for reactions of alkanals instead of alkanones ($\Delta\Delta G^{\ddagger}_{\text{C3one,i-C3al,i}}$ > 20 and 22 ± 1 kJ mol^{-1}, Table 3). Such benchmarking of theory and experiment confirms once again the adequacy of the theoretical methods and of the small TiO_2 model clusters used here to describe the energetics of C−C and C−O coupling reactions of enolate−carbonyl (enolate−alkanol) pairs for a broad range of oxygenates of practical interest in condensation and esterification reactions.

Table 7. DFT-Derived $\Delta G^{\ddagger}_{\text{C−C}}$ (kJ mol^{-1}) for Aldol Condensation between Ethanal, Propanal, Butanal, and Acetone and Their Respective Enolates[a]

	carbonyl reactant			
enolate reactant	ethanal	propanal	butanal	acetone
ethenolate	81	78	78	95
propen-1-olate	77	76	74	97
buten-1-olate	79	75	73	93
propen-2-olate	86	84	83	104

[a] On Ti_{5c}−O_{3c}−Ti_{5c} structures of the anatase $Ti_5O_{19}H_{18}$ cluster, B3LYP, 6-311G(d,p) for C, H, and O atoms, LANL2DZ for Ti atoms; 523 K, 1 bar.

C_2−C_4 alkanal reactants show similar $\Delta G^{\ddagger}_{\text{C−C}}$ values for C−C coupling reactions with a given enolate, irrespective of the enolate structure (Table 7). For instance, $\Delta G^{\ddagger}_{\text{C−C}}$ values for C−C coupling of propen-1-olates with C_2−C_4 alkanals decrease only slightly with increasing chain length (ethanal (77 kJ mol^{-1}); butanal (74 kJ mol^{-1})) in response to the stronger van der Waals interactions for longer alkyls, as also observed for self-condensation of linear alkanals (Table 6). These similar $\Delta G^{\ddagger}_{\text{C−C}}$ values for C_2−C_4 alkanal reactants reflect weak effects of the α-alkyl substituents on alkanal reactivity, consistent with the large distances between the α-alkyl substituent in alkanals and the alkyl group in the enolates at the C−C coupling transition states. For instance, the C−C distance between the terminal $-CH_3$ groups in propen-1-olate−propanal pairs (0.356 nm) are slightly larger than the combined van der Waals radii of the two C atoms (0.34 nm) (Scheme 13a).

As in the case of propanal and acetone reactions with propen-1-olates or propen-2-olates, all $\Delta\Delta G^{\ddagger}_{\text{C3one},i\text{-n},i}$ values (n = C2al (ethanol) or C4al (butanal); eq 25) for enolates (ethenolate, propen-1-olate, propen-2-olate, buten-1-olate) are large and positive (Table 7), indicative of the ubiquitous lower reactivity of alkanones in nucleophilic attack by enolates. The C−C coupling TS structures for reactions of propen-1-olate with propanal (Scheme 13a) and acetone (Scheme 13c) reflect the significant steric effects imposed by the second $-CH_3$ group at the acetone carbonyl C atom, which obstructs the position of the $-C_2H_5$ group at the α-C atom in propen-1-olate. These conclusions are consistent with the predominant contributions of nondispersive interactions ($\Delta\Delta H^{\ddagger}_{\text{unc,C−C}}$ 13 kJ mol^{-1}, section S11, SI) and of entropy terms ($-T\Delta\Delta S^{\ddagger}_{\text{C−C}}$ 13 kJ mol^{-1}, section S11, SI) to the $\Delta\Delta G^{\ddagger}_{\text{C3one},i\text{-C3al},i}$ values (21 kJ mol^{-1}, Table 7) for propen-1-olates.

DFT treatments can also probe enolate reactivity, a property inaccessible to experiment because of the low prevalent enolate coverages at all conditions of practical condensation and esterification catalysis. $\Delta G^{\ddagger}_{\text{C−C}}$ values (Table 7) show that enolates derived from C_2−C_4 alkanals have similar reactivities in C−C coupling reactions with a given alkanal or alkanone. For instance, these C_2−C_4 enolates react with propanal with $\Delta G^{\ddagger}_{\text{C−C}}$ values of 75−78 kJ mol^{-1} (Table 7), indicative of weak effects of enolate structure on reactivity and a specific insensitivity of C−C coupling reactivity with a given carbonyl coreactant to the nature of the alkyl substituents at the α-C atom.

Alkanone-derived enolates (e.g., propen-2-olate formed from acetone), in contrast, showed much larger $\Delta G^{\ddagger}_{\text{C−C}}$ values than those formed from alkanals (Table 7). For instance, the coupling of propanal with propen-2-olate has a $\Delta G^{\ddagger}_{\text{C−C}}$ value of 84 kJ mol^{-1}, while its reaction with propen-1-olate exhibits a free energy barrier of 75 kJ mol^{-1}. The $-C_2H_5$ group in propanal lies parallel to the C=C bond in propen-2-olate at the C−C coupling TS (Scheme 13d), so as to minimize steric repulsion by the $-CH_3$ group of the enolate. In contrast, this $-C_2H_5$ group is positioned in a nearly perpendicular position at the TS that mediates propanal reactions with propen-1-olate (Scheme 13a). The propen-1-olate−propanal TS places the $-C_2H_5$ group in propanal closer to the enolate than at the propen-2-olate−propanal TS, thus leading to more effective van der Waals stabilization of its C−C coupling TS ($\Delta\Delta H_{\text{vdw,C−C}}$ 7 kJ mol^{-1}, section S11, SI).

4. CONCLUSIONS

Enolate formation of carbonyl compounds (i.e., alkanals and alkanones) via cleavage of α-C−H bonds is a common kinetically relevant step for aldol condensation and esterification of alkanol−alkanal (alkanone) mixtures catalyzed by Lewis acid−base site pairs present on oxide surfaces. C−C coupling reactions of the formed enolates with coadsorbed alkanals (alkanones) and C−O coupling reactions of alkanal−alkoxide pairs (derived from H transfer between the enolates and coadsorbed alkanols) mediate selectivities of the enolates to form condensation or esterification products. These mechanistic conclusions are general for C_2−C_5 oxygenate reactants and for anatase TiO_2 and monoclinic ZrO_2, as evident from kinetic, isotopic, and theoretical assessments.

Enolate formation transition states at acid−base site pairs with moderate acid−base strength occur at an intermediate

DOI: 10.1021/acs.jpcc.6b07304
J. Phys. Chem. C 2016, 120, 21589−21616

point along the reaction coordinate, irrespective of alkyl substituents at the α-C or carbonyl C atoms in the reactants, and show concerted interactions of α-H atoms with basic lattice O sites and of the incipiently formed enolate moieties with acidic metal centers. The free energies of these enolate formation transition states are mediated by the heterolytic dissociation energy of α-C−H bonds and steric hindrance of α-alkyl groups to the abstraction of α-H atoms by the lattice O sites, leading to lower reactivities of alkanones than alkanals and to lower reactivities of alkanals with a longer or more branched α-alkyl group.

Alkyl groups in enolate−alkanal pairs at C−C coupling transition states are much closer with each other than those in alkanal−alkoxide pairs at C−O coupling transition states, leading to much stronger steric repulsion between alkyl groups for the C−C bond formation. As a result of these steric effects, the intrinsic esterification/condensation rate ratios of alkanol−alkanal reactants increase as the alkyl chains of the reactants lengthen or become more branched. These steric effects are also reflected in cross condensation of alkanals and alkanones; alkanones with two alkyl groups at the carbonyl C atom are less reactive than alkanals with a single alkyl group in C−C coupling reactions with enolates. H_2O provides an alternative way to mediate the esterification selectivity by acting as a cocatalyst, in which H_2O reacts with enolates to form 1,1-diols that undergo esterification with alkanols to give H_2O and hemiacetals (precursors of ester products) with lower free energy barriers than the direct C−O coupling reactions between enolates and alkanols to form the same hemiacetals.

Monoclinic ZrO_2 has weaker acid centers but stronger base sites than anatase TiO_2, resulting in more stable enolate formation transition states that benefit from stronger interactions between the base sites and the α-H atoms at the transition states. The two Zr centers in Zr−O−Zr structures on monoclinic ZrO_2 surfaces are very different in acid strength and lead to distinct esterification/condensation rate ratios for enolates bound to one of these Zr centers, as the relative stabilities of C−C and C−O coupling transition states (derived from an enolate and an alkanal or alkanol coreactant) depend on the interactions of these C−C and C−O coupling transition states with the enolate-bearing and coreactant-bearing Zr centers, respectively. This effect of asymmetric Zr centers leads to a weak dependence of measured esterification/condensation rate ratios on alkanol/alkanal reactant ratios, in contrast to the linear relations between these ratios observed on anatase TiO_2 surfaces, which have uniform Ti centers.

■ ASSOCIATED CONTENT

Ⓢ Supporting Information

The Supporting Information is available free of charge on the ACS Publications website at DOI: 10.1021/acs.jpcc.6b07304.

> Approach to equilibrium parameters for $C_2D_5OD-CD_3CDO-D_2$ mixtures at catalytic conditions; reversibility of adsorption of CO_2 and propanoic acid and acetone condensation rates and H/D isotopic effects on $ZrO_2(m)$; derivation of rate equations for $ZrO_2(m)$-catalyzed esterification and condensation reactions; comparison of enolate formation rates of carbonyl compounds in the presence or absence of other carbonyl reactants; effects of alkanol pressure on esterification rates of enolates with alkanol coreactants; effect of H_2O on the dehydrogenation function of Cu; DFT-derived H^+ affinities for carbonyl O atoms in C_2-C_5 carbonyl compounds; detailed DFT treatments of aldol condensation and esterification pathways using anatase $Ti_5O_{19}H_{18}$ cluster models, including optimized structures of reactants, transition states, and products involved in elementary steps, their enthalpies, entropies, and free energies, analyses of charge distribution for C−C and C−O coupling transition states, and pathways for reactions of enolates with H_2O (PDF)

■ AUTHOR INFORMATION

Corresponding Author

*Fax: + 1 510- 642-4778. E-mail: iglesia@berkeley.edu. Phone: 925-323-5559.

Notes

The authors declare no competing financial interest.

■ ACKNOWLEDGMENTS

We are grateful for thoughtful technical discussions with Drs. Eric Doskocil, John Shabaker, and Glenn Sunley and other members of the XC^2 program at BP p.l.c. We thank Drs. Stanley Herrmann, Prashant Deshlahra, and Elif Gurbuz at UC—Berkeley for their comments and advice throughout this study and also thank Dr. Yongchun Hong and Mr. Trenton Otto at UC—Berkeley for a careful review of this manuscript. We acknowledge the financial support from BP through the XC^2 program at UC—Berkeley. The computational resources provided by the Extreme Science and Engineering Discovery Environment (XSEDE) (NSF, grant no. ACI-1053575) and the Molecular Graphics and Computation Facility at UC—Berkeley (NSF, grant no. CHE-0840505) are also acknowledged with thanks.

■ REFERENCES

(1) Gines, M. J. L.; Iglesia, E. Bifunctional Condensation Reactions of Alcohols on Basic Oxides Modified by Copper and Potassium. *J. Catal.* **1998**, *176*, 155−172.

(2) Lin, F.; Chin, Y. Mechanism of Intra- and Inter-Molecular C═C Bond Formation of Propanal on Brønsted Acid Sites Contained within MFI Zeolites. *J. Catal.* **2014**, *311*, 244−256.

(3) Huber, G. W.; Iborra, S.; Corma, A. Synthesis of Transportation Fuels from Biomass: Chemistry, Catalysts, and Engineering. *Chem. Rev.* **2006**, *106*, 4044−4098.

(4) Simonetti, D. A.; Dumesic, J. A. Catalytic Production of Liquid Fuels from Biomass-Derived Oxygenated Hydrocarbons: Catalytic Coupling at Multiple Length Scales. *Catal. Rev.: Sci. Eng.* **2009**, *51*, 441−484.

(5) Serrano-Ruiz, J. C.; West, R. M.; Dumesic, J. A. Catalytic Conversion of Renewable Biomass Resources to Fuels and Chemicals. *Annu. Rev. Chem. Biomol. Eng.* **2010**, *1*, 79−100.

(6) Kunkes, E. L.; Simonetti, D. A.; West, R. M.; Serrano-Ruiz, J. C.; Gartner, C. A.; Dumesic, J. A. Catalytic Conversion of Biomass to Monofunctional Hydrocarbons and Targeted Liquid-Fuel Classes. *Science* **2008**, *322*, 417−421.

(7) Yang, J.; Li, N.; Li, G.; Wang, W.; Wang, A.; Wang, X.; Cong, Y.; Zhang, T. Synthesis of Renewable High-Density Fuels Using Cyclopentanone Derived from Lignocellulose. *Chem. Commun. (Cambridge, U. K.)* **2014**, *50*, 2572−2574.

(8) Anbarasan, P.; Baer, Z. C.; Sreekumar, S.; Gross, E.; Binder, J. B.; Blanch, H. W.; Clark, D. S.; Toste, F. D. Integration of Chemical Catalysis with Extractive Fermentation to Produce Fuels. *Nature* **2012**, *491*, 235−239.

(9) Bankar, S. B.; Survase, S. A.; Ojamo, H.; Granström, T. The Two Stage Immobilized Column Reactor with an Integrated Solvent

Recovery Module for Enhanced ABE Production. *Bioresour. Technol.* **2013**, *140*, 269−276.

(10) Nielsen, A.; Houlihan, W. The Aldol Condensation. *Org. React.* **1968**, *16*, 1−438.

(11) Du, J.; Say, R. F.; Lü, W.; Fuchs, G.; Einsle, O. Active-Site Remodelling in the Bifunctional Fructose-1,6-Bisphosphate Aldolase/Phosphatase. *Nature* **2011**, *478*, 534−538.

(12) Zeidan, R. K.; Hwang, S.; Davis, M. E. Multifunctional Heterogeneous Catalysts: SBA-15-Containing Primary Amines and Sulfonic Acids. *Angew. Chem., Int. Ed.* **2006**, *45*, 6332−6335.

(13) Collier, V. E.; Ellebracht, N. C.; Lindy, G. I.; Moschetta, E. G.; Jones, C. W. Kinetic and Mechanistic Examination of Acid−Base Bifunctional Aminosilica Catalysts in Aldol and Nitroaldol Condensations. *ACS Catal.* **2016**, *6*, 460−468.

(14) Iglesia, E.; Barton, D. G.; Biscardi, J. A.; Gines, M. J. L.; Soled, S. L. Bifunctional Pathways in Catalysis by Solid Acids and Bases. *Catal. Today* **1997**, *38*, 339−360.

(15) Di Cosimo, J. I.; Díez, V. K.; Apesteguía, C. R. Base Catalysis for the Synthesis of *α,β*-Unsaturated Ketones from the Vapor-Phase Aldol Condensation of Acetone. *Appl. Catal., A* **1996**, *137*, 149−166.

(16) Shen, W.; Tompsett, G. A.; Xing, R.; Conner, W. C., Jr.; Huber, G. W. Vapor Phase Butanal Self-Condensation over Unsupported and Supported Alkaline Earth Metal Oxides. *J. Catal.* **2012**, *286*, 248−259.

(17) Di Cosimo, J. I.; Apesteguía, C. R.; Ginés, M. J. L.; Iglesia, E. Structural Requirements and Reaction Pathways in Condensation Reactions of Alcohols on Mg_yAlO_x Catalysts. *J. Catal.* **2000**, *190*, 261−275.

(18) Di Cosimo, J. I.; Torres, G.; Apesteguía, C. R. One-Step MIBK Synthesis: A New Process from 2-Propanol. *J. Catal.* **2002**, *208*, 114−123.

(19) Torres, G.; Apesteguía, C. R.; Di Cosimo, J. I. One-Step Methyl Isobutyl Ketone (MIBK) Synthesis from 2-Propanol: Catalyst and Reaction Condition Optimization. *Appl. Catal., A* **2007**, *317*, 161−170.

(20) Nikolopoulos, A. A.; Jang, B. W.-L.; Spivey, J. J. Acetone Condensation and Selective Hydrogenation to MIBK on Pd and Pt Hydrotalcite-Derived Mg−Al Mixed Oxide Catalysts. *Appl. Catal., A* **2005**, *296*, 128−136.

(21) Kunkes, E. L.; Gürbüz, E. I.; Dumesic, J. A. Vapour-Phase C−C Coupling Reactions of Biomass-Derived Oxygenates over Pd/$CeZrO_x$ Catalysts. *J. Catal.* **2009**, *266*, 236−249.

(22) Gangadharan, A.; Shen, M.; Sooknoi, T.; Resasco, D. E.; Mallinson, R. G. Condensation Reactions of Propanal over $Ce_xZr_{1-x}O_2$ Mixed Oxide Catalysts. *Appl. Catal., A* **2010**, *385*, 80−91.

(23) Sun, J.; Baylon, R. A. L.; Liu, C.; Mei, D.; Martin, K. J.; Venkitasubramanian, P.; Wang, Y. Key Roles of Lewis Acid−Base Pairs on $Zn_xZr_yO_z$ in Direct Ethanol/Acetone to Isobutene Conversion. *J. Am. Chem. Soc.* **2016**, *138*, 507−517.

(24) Hanna, D. G.; Shylesh, S.; Li, Y.; Krishna, S.; Head-Gordon, M.; Bell, A. T. Experimental and Theoretical Study of *n*-Butanal Self-Condensation over Ti Species Supported on Silica. *ACS Catal.* **2014**, *4*, 2908−2916.

(25) Rekoske, J. E.; Barteau, M. A. Kinetics, Selectivity, and Deactivation in the Aldol Condensation of Acetaldehyde on Anatase Titanium Dioxide. *Ind. Eng. Chem. Res.* **2011**, *50*, 41−51.

(26) Luo, S.; Falconer, J. L. Acetone and Acetaldehyde Oligomerization on TiO_2 Surfaces. *J. Catal.* **1999**, *185*, 393−407.

(27) Barteau, M. A. Organic Reactions at Well-Defined Oxide Surfaces. *Chem. Rev.* **1996**, *96*, 1413−1430.

(28) Zaki, M. I.; Hasan, M. A.; Pasupulety, L. Surface Reactions of Acetone on Al_2O_3, TiO_2, ZrO_2, and CeO_2: IR Spectroscopic Assessment of Impacts of the Surface Acid−Base Properties. *Langmuir* **2001**, *17*, 768−774.

(29) Singh, M.; Zhou, N.; Paul, D. K.; Klabunde, K. J. IR Spectral Evidence of Aldol Condensation: Acetaldehyde Adsorption over TiO_2 Surface. *J. Catal.* **2008**, *260*, 371−379.

(30) Wang, S.; Iglesia, E. Condensation and Esterification Reactions of Alkanals, Alkanones, and Alkanols on TiO_2: Elementary Steps, Site Requirements, and Synergistic Effects of Bifunctional Strategies. *J. Catal.* **2016**, *340*, 302−320.

(31) An, W. The Role of Synergic Interaction in Transition State Formation for the Aldol Reaction on a Metal Oxide Catalyst: A DFT Investigation. *Phys. Chem. Chem. Phys.* **2015**, *17*, 22529−22532.

(32) Li, W.; Huang, H.; Li, H.; Zhang, W.; Liu, H. Facile Synthesis of Pure Monoclinic and Tetragonal Zirconia Nanoparticles and Their Phase Effects on the Behavior of Supported Molybdena Catalysts for Methanol-Selective Oxidation. *Langmuir* **2008**, *24*, 8358−8366.

(33) Pacchioni, G. Ketonization of Carboxylic Acids in Biomass Conversion over TiO_2 and ZrO_2 Surfaces: A DFT Perspective. *ACS Catal.* **2014**, *4*, 2874−2888.

(34) Panchenko, V. N.; Zaytseva, Yu. A.; Simonov, M. N.; Simakova, I. L.; Paukshtis, E. A. DRIFTS and UV−vis DRS Study of Valeric Acid Ketonization Mechanism over ZrO_2 in Hydrogen Atmosphere. *J. Mol. Catal. A: Chem.* **2014**, *388−389*, 133−140.

(35) Frisch, M. J.; Trucks, G. W.; Schlegel, H. B.; Scuseria, G. E.; Robb, M. A.; Cheeseman, J. R.; Scalmani, G.; Barone, V.; Mennucci, B.; Petersson, G. A., et al. *Gaussian 09*, Revision D.01; Gaussian, Inc.: Wallingford, CT, 2009.

(36) Li, X.; Frisch, M. J. Energy-Represented Direct Inversion in the Iterative Subspace within a Hybrid Geometry Optimization Method. *J. Chem. Theory Comput.* **2006**, *2*, 835−839.

(37) Becke, A. D. Density−Functional Thermochemistry. III. The Role of Exact Exchange. *J. Chem. Phys.* **1993**, *98*, 5648−5652.

(38) Lee, C.; Yang, W.; Parr, R. G. Development of the Colle-Salvetti Correlation-Energy Formula into a Functional of the Electron Density. *Phys. Rev. B: Condens. Matter Mater. Phys.* **1988**, *37*, 785−789.

(39) McLean, A. D.; Chandler, G. S. Contracted Gaussian Basis Sets for Molecular Calculations. I. Second Row Atoms, Z = 11−18. *J. Chem. Phys.* **1980**, *72*, 5639−5648.

(40) Krishnan, R.; Binkley, J. S.; Seeger, R.; Pople, J. A. Self−Consistent Molecular Orbital Methods. XX. A Basis Set for Correlated Wave Functions. *J. Chem. Phys.* **1980**, *72*, 650−654.

(41) Hay, P. J.; Wadt, W. R. *Ab Initio* Effective Core Potentials for Molecular Calculations. Potentials for the Transition Metal Atoms Sc to Hg. *J. Chem. Phys.* **1985**, *82*, 270−283.

(42) Grimme, S.; Ehrlich, S.; Goerigk, L. Effect of the Damping Function in Dispersion Corrected Density Functional Theory. *J. Comput. Chem.* **2011**, *32*, 1456−1465.

(43) Boys, S. F.; Bernardi, F. The Calculation of Small Molecular Interactions by the Differences of Separate Total Energies. Some Procedures with Reduced Errors. *Mol. Phys.* **1970**, *19*, 553−566.

(44) Simon, S.; Duran, M.; Dannenberg, J. J. How Does Basis Set Superposition Error Change the Potential Surfaces for Hydrogen−Bonded Dimers? *J. Chem. Phys.* **1996**, *105*, 11024−11031.

(45) McQuarrie, D. A. *Statistical Mechanics*; University Science Books: Sausalito, CA, 2000.

(46) Merrick, J. P.; Moran, D.; Radom, L. An Evaluation of Harmonic Vibrational Frequency Scale Factors. *J. Phys. Chem. A* **2007**, *111*, 11683−11700.

(47) Grimme, S. Supramolecular Binding Thermodynamics by Dispersion-Corrected Density Functional Theory. *Chem. - Eur. J.* **2012**, *18*, 9955−9964.

(48) Wiberg, K. A. Application of the Pople-Santry-Segal CNDO Method to the Cyclopropylcarbinyl and Cyclobutyl Cation and to Bicyclobutane. *Tetrahedron* **1968**, *24*, 1083−1096.

(49) Mayer, I. Bond Order and Valence Indices: A Personal Account. *J. Comput. Chem.* **2007**, *28*, 204−221.

(50) Martin, R. L. Natural Transition Orbitals. *J. Chem. Phys.* **2003**, *118*, 4775−4777.

(51) Pulido, A.; Oliver-Tomas, B.; Renz, M.; Boronat, M.; Corma, A. Ketonic Decarboxylation Reaction Mechanism: A Combined Experimental and DFT Study. *ChemSusChem* **2013**, *6*, 141−151.

(52) Kresse, G.; Hafner, J. *Ab Initio* Molecular Dynamics for Liquid Metals. *Phys. Rev. B: Condens. Matter Mater. Phys.* **1993**, *47*, 558−561.

(53) Kresse, G.; Furthmuller, J. Efficiency of *Ab-Initio* Total Energy Calculations for Metals and Semiconductors using a Plane-Wave Basis Set. *Comput. Mater. Sci.* **1996**, *6*, 15−50.

(54) Kresse, G.; Furthmuller, J. Efficient Iterative Schemes for *Ab Initio* Total-Energy Calculations using a Plane-Wave Basis Set. *Phys. Rev. B: Condens. Matter Mater. Phys.* **1996**, *54*, 11169−11186.

(55) Perdew, J. P.; Burke, K.; Ernzerhof, M. Generalized Gradient Approximation Made Simple. *Phys. Rev. Lett.* **1996**, *77*, 3865−3868.

(56) Perdew, J. P.; Burke, K.; Ernzerhof, M. Generalized Gradient Approximation Made Simple [Phys. Rev. Lett. 77, 3865 (1996)]. *Phys. Rev. Lett.* **1997**, *78*, 1396.

(57) Blöchl, P. E. Projector Augmented-Wave Method. *Phys. Rev. B: Condens. Matter Mater. Phys.* **1994**, *50*, 17953−17979.

(58) Kresse, G.; Joubert, D. From Ultrasoft Pseudopotentials to the Projector Augmented-Wave Method. *Phys. Rev. B: Condens. Matter Mater. Phys.* **1999**, *59*, 1758−1775.

(59) Monkhorst, H. J.; Pack, J. D. Special Points for Brillouin-Zone Integrations. *Phys. Rev. B* **1976**, *13*, 5188−5192.

(60) Howard, C. J.; Hill, R. J.; Reichert, B. E. Structures of ZrO_2 Polymorphs at Room Temperature by High-Resolution Neutron Powder Diffraction. *Acta Crystallogr., Sect. B: Struct. Sci.* **1988**, *44*, 116−120.

(61) Birch, F. Finite Elastic Strain of Cubic Crystals. *Phys. Rev.* **1947**, *71*, 809−824.

(62) Makov, G.; Payne, M. C. Periodic Boundary Conditions in *Ab Initio* Calculations. *Phys. Rev. B: Condens. Matter Mater. Phys.* **1995**, *51*, 4014−4022.

(63) Neugebauer, J.; Scheffler, M. Adsorbate-Substrate and Adsorbate-Adsorbate Interactions of Na and K Adlayers on Al(111). *Phys. Rev. B: Condens. Matter Mater. Phys.* **1992**, *46*, 16067−16080.

(64) Grimme, S. Semiempirical GGA-Type Density Functional Constructed with a Long-Range Dispersion Correction. *J. Comput. Chem.* **2006**, *27*, 1787−1799.

(65) Stull, D. R.; Westrum, E. F.; Sinke, G. C. *The Chemical Thermodynamics of Organics Compounds*; John Wiley & Sons, Inc.: New York, 1969.

(66) Chiang, Y.; Hojatti, M.; Keeffe, J. R.; Kresge, A. J.; Schepp, N. P.; Wirz, J. Vinyl Alcohol. Generation and Decay Kinetics in Aqueous Solution and Determination of the Tautomerization Equilibrium Constant and Acid Dissociation Constants of the Aldehyde and Enol Forms. *J. Am. Chem. Soc.* **1987**, *109*, 4000−4009.

(67) Guthrie, J. P. Rate-Equilibrium Correlations for the Aldol Condensation: An Analysis in Terms of Marcus Theory. *J. Am. Chem. Soc.* **1991**, *113*, 7249−7255.

(68) Santen, R. A. V.; Neurock, M.; Shetty, S. G. Reactivity Theory of Transition-Metal Surfaces: A Brønsted−Evans−Polanyi Linear Activation Energy−Free-Energy Analysis. *Chem. Rev.* **2010**, *110*, 2005−2048.

DOI: 10.1021/acs.jpcc.6b07304
J. Phys. Chem. C 2016, 120, 21589−21616